Remote Sensing of Environment 282 (2022) 113270

Contents lists available at ScienceDirect

Remote Sensing of Environment

journal homepage: www.elsevier.com/locate/rse

Monitoring of high biomass *Phaeocystis globosa* blooms in the Southern North Sea by in situ and future spaceborne hyperspectral radiometry

Héloïse Lavigne *, Kevin Ruddick, Quinten Vanhellemont

Royal Belgium Institute for Natural Sciences (RBINS), Brussels, Belgium

ARTICLE INFO

Edited by Dr. Menghua Wang

Keywords:
Phaeocystis globosa
Hyperspectral radiometry
Autonomous measurements
PANTHYR
Belgian coastal zone
Hyperspectral satellite sensors
Inter-band calibration
Signal to noise ratio

ABSTRACT

Phaeocystis globosa (*P. globosa* hereafter) is a phytoplankton species which commonly blooms at high biomass in April–May in the Southern North Sea and forms undesirable foam which accumulates on the beaches. Monitoring of this species is required by EU directives. Measurement of phytoplankton species composition has historically been made by pigment or microscopic analysis of water samples, which is spatially sparse and temporally infrequent e.g. weekly/monthly. In-water instruments such as flow cytometers can provide very high frequency data but at high acquisition and maintenance cost. Automated in situ above water radiometry has the potential to provide very high frequency data at single locations but requires very careful design of processing algorithms in turbid waters with high non-algal absorption. Spaceborne radiometry could provide both very good spatial coverage and moderate/high frequency of data, e.g. daily/weekly, but accurate determination of phytoplankton species composition is considerably more difficult in turbid waters than in open ocean waters. Prior studies based on a limited number of shipborne reflectance measurements suggested feasibility of *P. globosa* detection in turbid waters from hyperspectral radiometry. The availability of a new autonomous above water hyperspectral radiometer system has enabled further refinement and intensive testing of these techniques. From a time-series of 4356 water reflectance spectra measured near Ostend harbour in Belgian coastal waters from 2020/04/01 to 2020/08/18, two existing algorithms for *P. globosa* detection were successfully applied. Results show a high biomass *P. globosa* bloom occurring in late-April/early-May as found every year in water sample analyses for Belgian coastal waters. The high temporal resolution of the radiometric data allows to capture the evolution of the bloom at time scales sufficiently short (hourly and daily) compared to growth/decay and tidal processes.

The challenges of extending the methods to future spaceborne instruments are also tested by simulating the impact of errors in sensor inter-band calibration, atmospheric correction and radiometric noise. Results show that because of their spectral coherence, atmospheric correction errors impact only slightly *P. globosa* detection whereas inaccuracy in inter-band calibration and radiometric noise are much more problematic as they affect each spectral band independently. Because radiometric noise should be reduced in the new generation of hyperspectral sensors and can always be reduced by spatial binning, the inter-band relative calibration uncertainty appears to be the main challenge for spaceborne mission design. Indeed, it was demonstrated that inter-band calibration error should be <0.25% and ideally 0.1% at top of the atmosphere highlighting the need for particular attention to inter-band calibration in sensor design and post processing treatments including vicarious calibration.

1. Introduction

The prymnesiophyte *Phaeocystis globosa* (*P. globosa* hereafter) is a phytoplankton species that blooms every spring in the Southern North Sea (SNS, hereafter). Exponential *P. globosa* growth is known to occur after a primary bloom of diatoms in Belgian waters and to be favoured by nitrate enrichment from rivers (Lancelot, 1995; Lancelot et al., 1998; Lacroix et al., 2007). During blooms, *P. globosa* has the ability to form colonies of hundreds of cells embedded in a polysaccharide gel matrix which provides them a competitive advantage to reduce predation (Rousseau et al., 2007). In addition, *P. globosa* is able to transform organic phosphate which allows it to grow in inorganic phosphate depleted waters (Veldhuis et al., 1986; Blauw et al., 2010).

Although *P. globosa* is not toxic, it does impact ecosystem and

* Corresponding author.
E-mail address: hlavigne@naturalsciences.be (H. Lavigne).

https://doi.org/10.1016/j.rse.2022.113270
Received 4 April 2022; Received in revised form 6 September 2022; Accepted 9 September 2022
Available online 29 September 2022

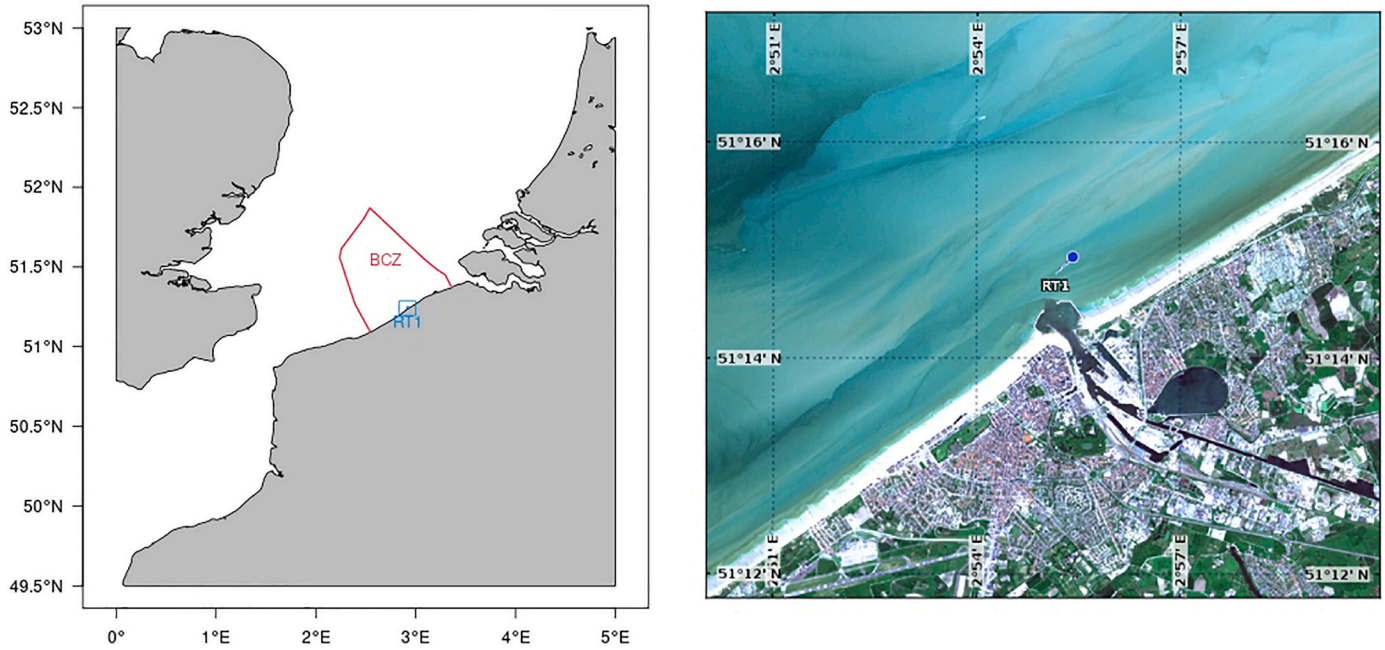

Fig. 1. Left: general map of the Southern North Sea with the boundaries of the Belgian Coastal Zone in red. RT1 Location is indicated by the blue dot in the blue square. Right: a larger view of the blue square (left panel) from the RGB image of Sentinel 2-MSI sensor taken on 2018-05-04. (For interpretation of the references to colour in this figure legend, the reader is referred to the web version of this article.)

economic activities. Because of its polysaccharide matrix that is almost not grazed by zooplankton (Schoemann et al., 2005), *P. globosa* contributes strongly to a microbial food chain with much lower trophic efficiency than the linear food chain with grazing on diatoms (Rousseau et al., 2000), and hence affects fisheries. Aquaculture activities can also be affected. For example, a mass mussel mortality event was attributed to a *P. globosa* bloom and explained by post-bloom anoxic conditions (Peperzak and Poelman, 2008). Finally, the deposition of foam on the beaches associated to *P. globosa* blooms and local current and wind conditions presents some inconveniences for touristic and economic activities (Lancelot, 1995). It is even occasionally a life-threatening environment for windsurfers (Philippart et al., 2020). Consequently, the OSPAR (Oslo and Paris Commission for the Prevention of Marine Pollution) procedure which aims to assess the eutrophication status of the European waters requires monitoring of this species.

Until now, *P. globosa* monitoring has been essentially based on in situ water sampling (Lancelot et al., 1987; Mills et al., 1994; Muylaert et al., 2006) and modelling efforts (Lancelot et al., 2005; Breton et al., 2006; Lacroix et al., 2007; Chen and Mynett, 2006; Blauw et al., 2010). More recently, high temporal observations were available from spectrofluorometric methods (Houliez et al., 2012) and flow cytometry (Bonato et al., 2016). For a full spatial coverage of the North Sea, the use of satellite ocean colour data presents a clear advantage. Indeed, such data is routinely used for the monitoring of chlorophyll-a concentration and eutrophication in the North Sea (Van der Zande et al., 2019a). However, although bulk phytoplankton biomass is well assessed from space via the chlorophyll-a concentration, to discriminate different phytoplankton species is much more challenging, especially in turbid waters (Bracher et al., 2017). Focusing on specific absorption or scattering properties associated to certain species it is sometime possible to propose species-specific algorithms feasible from space (Simis et al., 2005; Cannizzaro et al., 2008; Miller et al., 2006; Kurekin et al., 2014; Gokul and Shanmugam, 2016). Regarding *P. globosa*, Lubac et al. (2008) and Kurekin et al. (2014) proposed detection algorithms for multispectral MODIS and MERIS sensors. However, as for many species-specific algorithms based on multispectral data, the results are limited by the low spectral resolution. Indeed, in most of the cases, a certain phytoplankton species is identified by specificities in its pigment composition. Since pigment absorption peaks are narrow (Bidigare et al., 1990) a high spectral resolution is needed (Vandermeulen et al., 2017).

In the Southern North Sea, the chlorophyll-c_3 (Chl-c_3 hereafter) pigment was found to be a good indicator for *P. globosa* (Antajan et al., 2004). Based on this observation, *P. globosa* detection algorithms using water reflectance were proposed by Lubac et al. (2008) and Astoreca et al. (2009). Both algorithms are based on water reflectance anomalies in the 450 nm - 500 nm spectral range with in vivo chlorophyll-c (Chl-c hereafter) absorption peak at around 460 nm (Bidigare et al., 1990, September); Hoepffner and Sathyendranath, 1991). The Lubac et al. (2008) algorithm is based on anomalies in local maxima of the second derivative and Astoreca et al. (2009) on a line height difference algorithm, designed to be insensitive to non-algal particle (NAP) and Coloured Dissolved Organic Matter (CDOM) absorption. It is shown in Appendix A that a baseline algorithm is mathematically equivalent to a second derivative evaluated at a single wavelength. Because second order derivatives are quite insensitive to constituents with smooth spectral variation such as NAP and CDOM absorption, but do highlight narrow wavelength band changes in convexity of reflectance spectra, they are commonly used in the analysis of pigment composition (Bidigare et al., 1989).

Until recently, these two algorithms could not be applied to remote sensing satellites as the first generation of hyperspectral sensors (e.g. HICO, HYPERION, CHRIS) suffered from calibration problems and had too low sensitivity for aquatic applications (Devred et al., 2013; Dierssen et al., 2020). Li et al. (2021) did successfully apply the Lubac et al. (2008) algorithm on airborne hyperspectral measurements. With the development of new spaceborne spectrometers containing a large number of narrow bands in visible and near-infrared (e.g. the current PRISMA and DESIS and future EnMAP, PACE, SBG, CHIME, GLIMR), *P. globosa* bloom detection in the Southern North Sea can now be reconsidered.

To support future hyperspectral sensors but also validate the multitude of satellite-based spectrometers with different spectral properties, autonomous hyperspectral measurement systems have been developed (Vansteenwegen et al., 2019; Goyens et al., 2018). A PAN-and-Tilt

HYperspectral Radiometer (PANTHYR) prototype system (Vansteenwegen et al., 2019) has been deployed in Belgian coastal waters near Ostend harbour and continuously measured water leaving radiance reflectance from December 2019 to August 2020. From this unique dataset, we first aim to test the feasibility of monitoring the *P. globosa* bloom from radiometric data. Then, potential errors associated with satellite measurements were simulated to determine under which conditions the *P. globosa* bloom could be monitored from satellite data. In particular, the impact of errors in inter-band relative calibration, atmospheric correction error and radiometric noise were tested.

The PANTHYR dataset, *P. globosa* algorithms and methods used to simulate satellite measurement errors are presented in the next section. Results are presented and briefly discussed in Section 3. A deeper discussion based on future satellite capabilities is provided in Section 4.

2. Data and methods

2.1. Study region – Belgian Coastal Zone (BCZ)

In situ reflectance data were collected by a prototype PANTHYR system (Vansteenwegen et al., 2019) deployed on the Blue Innovative Platform Research Tower 1 (51.2464°N, 2.9193°E), 500 m offshore of Ostend harbour in the Belgian Coastal Zone (BCZ, see Fig. 1). The hydrography of the BCZ is dominated by Atlantic water which inflows from the Channel (Lacroix et al., 2004) and is advected by very strong alongshore tidal currents which cause sediment resuspension and high turbidity. Suspended particulate matter concentration ranges from <1 g m^{-3} in offshore and deep waters to >100 g m^{-3} in very shallow water. Nutrient concentrations are high in winter, ranging from 20 μM to 80 μM, 0.5 μM to 1.5 μM and 4 μM to 10 μM for nitrates, phosphates and silicates, respectively Brion et al. (2008). Redfield et al. (1963) stochiometric ratios indicating averaged nutrient ratio in the global ocean and best nutrient ratios for diatoms growth are not respected. Indeed, BCZ water are comparatively enriched in nitrate and phosphate compared to silicates. Unbalanced nutrient ratios are explained by the high concentration of anthropogenic nitrate and phosphate in main rivers flowing into the BCZ and adjacent coastal waters (Brion et al., 2008). Phytoplankton blooms characterized by high Chl-a concentration (often higher than 10 mg m^{-3}) develop at spring in March in the clearest waters and in April/May in almost the entire BCZ. The growing season which lasts from March–April to October is mostly dominated by two taxa: diatoms and *P. globosa* (Muylaert et al., 2006). Whereas diatoms are present during the full season, *P. globosa* blooms for about 4 to 8 weeks in April–May when the lack of silicates is limiting diatom growth (Breton et al., 2006).

2.2. Radiometric data analysis

2.2.1. In situ water reflectance data

The PANTHYR system is composed of two TriOS/RAMSES radiometers for radiance and irradiance respectively mounted on a pan-and-tilt base which allows for continuous radiometric measurements at specified relative azimuth to sun. A typical measurement which lasts for about one minute is composed of 3 scans for spectral downwelling irradiance (E_d), 3 scans for downwelling radiance (L_d) and 11 scans for upwelling radiance (L_u), 3 more scans for downwelling radiance and 3 more scans for spectral downwelling irradiance. Measurements were performed from December 11th 2019 to August 18th 2020 every 20 min from sunrise to sunset for relative azimuth angles of 270° and 225° away from sun. Radiance and irradiance spectra were binned on a regular spectral grid ranging from 350 nm to 900 nm with steps of 2.5 nm and controlled according to Ruddick et al. (2006). If L_d and L_u scans showed >25% difference with neighboring scans at 550 nm, they were removed. Similarly, E_d scans normalized by $\cos(\theta_s)$ were deleted if they presented >25% difference with neighboring scans. The water leaving radiance-reflectance (ρ_{wm}, hereafter) was then calculated if at least 9 scans out of 11 remained for E_d if at least 5 scans out of 6 remained for L_u and L_d. ρ_{wm} was computed from

$$\rho_{wm} = \frac{\pi\left(L_u - \rho_f L_d\right)}{E_d} \quad (1)$$

where ρ_f, the effective Fresnel coefficient is obtained from Mobley (1999) using wind speed estimations from the National Centers for Environmental Prediction (NCEP) 1-degree global model. A final quality control was applied to remove spectra with cloudy sky ($L_d/E_d > 0.05$ sr^{-1} at 750 nm, Ruddick et al., 2006), with a solar zenith angle higher than 75° and with invalid reflectance values in NIR. For the last test, if reflectance at 900 nm was higher than half of the maximum reflectance over the whole spectra, the full reflectance spectra was removed. These last three steps in quality control led to remove 45% of water reflectance spectra. The final dataset contains 5880 spectra from the full period and 4356 spectra for the period of interest for phytoplankton blooms (i.e. 2020-04-01 – 2020-08-18). Quality control on PANTHYR data is also described by Vansteenwegen et al. (2019) and Vanhellemont and Ruddick (2021).

2.2.2. In situ data for validation

The dataset collected during the HYPERMAQ project cruises and distributed on the pangaea platform (https://www.pangaea.de/) has been used (Castagna et al., 2022a) for algorithm validation. This dataset includes water reflectance measurements made from above radiance/irradiance measurements with a set of TriOS sensors and phytoplankton abundance estimation from DNA metabarcoding. DNA metabarcoding allows for the identification and for an estimation of the abundance of phytoplankton species thanks to DNA sequencing and recognition of key sequences corresponding to “Amplicon Single Variant” (ASV). Data are given in relative abundance corresponding to the ASV count aggregated to species relative to the total counts of eukaryotic phytoplankton (see Castagna et al., 2022b for a complete description of the protocols). From this dataset only the measurements made in the Belgian Coastal waters were used. During two cruises, in April (23–25/04/2018) and July (25/07/2018). the same region was sampled each time (latitudes: 51.18°N-51.59°N; longitudes: 2.50–3.15) and [Chl-a] ranged from 2.9 to 17.3 mg m^{-3} in April and from 1.9 to 9.9 mg m^{-3} in July. The final dataset contains 14 observations, 9 in April and 5 in July.

2.2.3. Calculation of P. globosa indexes

Astoreca et al. (2009) and Lubac et al. (2008) proposed algorithms for *P. globosa* in the Southern North Sea. The Lubac et al. (2008) algorithm indicates if the phytoplankton community is dominated by *P. globosa* (yes/no) and is based on the wavelength of local maxima and minima in the second derivative of the water reflectance. Analyzing the second derivative of water reflectance from measurements in the North Sea, that study demonstrated a shift in the wavelength of local maxima in the range 460 nm – 480 nm varying with the proportion of *P. globosa* in the phytoplankton community. Local maxima were observed around 475 nm when *P. globosa* was dominant and around 465 nm in the absence of *P. globosa*. Similarly, local minima expected in the range 480 nm – 510 nm were shifted to about 503 nm in samples when *P. globosa* was dominant compared to 485 nm in the absence of *P. globosa*. By defining threshold limits for the wavelength of second derivative reflectance maxima and minima, Lubac et al. (2008) were able to determine *P. globosa* dominated waters. These spectral features are explained by the presence of the Chl-c_3 as well as the low ratio of photoprotective carotenoids compared to total Chl-c (Lubac et al., 2008; Castagna et al., 2021).

Although focusing on the same signal in water reflectance spectra, Astoreca et al. (2009) proposed a different approach allowing the calculation of Chl-c_3 absorption with an analytical algorithm. This algorithm is based on a Line Height Difference (LHD) method applied to inverse reflectance normalized by NIR reflectance to yield absorption.

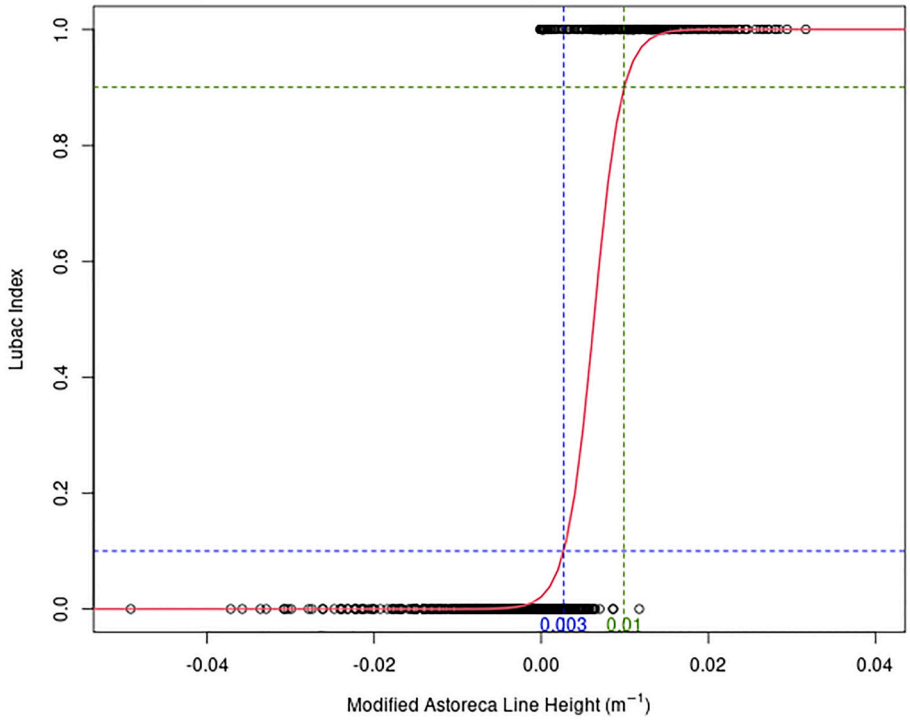

Fig. 2. Logit regression model (red curve) between the absence (LI = 0) or dominance (LI = 1) of *P. globosa* according to Lubac Index and the MALH values. Black circles show individual datapoints. Blue and green dotted lines refer respectively to the 0.1 and 0.9 probability values in the regression model and the corresponding threshold values for MALH. (For interpretation of the references to colour in this figure legend, the reader is referred to the web version of this article.)

The extra absorption due to Chl-c_3 is estimated from the difference between inverse reflectance at 467 nm and a baseline calculated from inverse reflectance at 450 nm and 480 nm, using an exponential baseline to better remove NAP and CDOM absorption. However, the central wavelength 467 nm which is supposed to represent the maximum of Chl-c_3 absorption can be suboptimal. Indeed, Lubac et al. (2008) shows that the second derivative of reflectance spectra for waters dominated by *P. globosa* or by diatoms diverge most in the 470–490 nm spectral range. More recently, Castagna et al. (2021) concluded from the analysis of in situ measurements in the North Sea that the Astoreca et al. (2009) algorithm rather targets total Chl-c absorption. As this simple 3 bands LHD algorithm could be more adapted to remote sensing hyperspectral sensor with a moderate spectral resolution (~ 10 nm), it was decided to keep the Astoreca et al. (2009) algorithm for *P. globosa* index calculation but to modify the spectral band triplet. In order to better capture reflectance difference between main diatoms groups expected in the SNS and *P. globosa* due to divergent Chl-c_3 and photoprotective carotenoids patterns, the original triplet 450 nm / 467.5 nm / 480 nm proposed in Astoreca et al. (2009) is modified here to 470 nm / 482.5 nm / 490 nm. This triplet should avoid disturbances due to chlorophyll-c_1 and c_2 absorption, as the analysis of the second derivative of water reflectance provided by Lubac et al., 2008, Fig. 4B) shows that in the 470 nm – 490 nm range, the second derivative is positive for *P. globosa* whereas negative for diatoms. A positive (negative) second derivative indicates that reflectance spectrum is convex (concave), which suggests the presence (absence) of extra absorption in this range. However, this modified algorithm cannot be considered anymore as a measure of extra Chl-c_3 absorption but rather as an absorption anomaly at 482.5 nm.

Following the Lubac et al. (2008) methodology, the second derivatives (eq. 3) have been calculated after 5-point window (12.5 nm) running average (eq. 2).

$$\overline{\rho_w}(\lambda_i) = \frac{1}{5}\sum_{j=i-2}^{j=i+2}\rho_w(\lambda_j), \tag{2}$$

$$\frac{d^2\overline{\rho_w}}{d\lambda^2} = \frac{\overline{\rho_w}(\lambda_{i+1}) - 2\overline{\rho_w}(\lambda_i) + \overline{\rho_w}(\lambda_{i-1})}{(\Delta\lambda)^2}, \tag{3}$$

In eq. (3), $\Delta\lambda = \lambda_i - \lambda_{i-1} = 2.5$ nm. Then, the wavelength of local maximum and local minimum are sought in the 460 nm - 480 nm and 480 nm - 510 nm intervals respectively. If the local maximum is observed in the range 471 nm - 480 nm and the local minimum is observed in 499 nm - 510 nm interval, the reflectance spectrum is identified as being dominated by *P. globosa*.

The modified Astoreca et al. (2009) line height difference (MALH hereafter) has been calculated with the original equation but with the shifted wavelengths as follows:

$$MALH = \left(\frac{1}{\rho_w(\lambda_2)} - \frac{1}{\rho_w(\lambda_1)^{(1-w)}} \bullet \frac{1}{\rho_w(\lambda_3)^w}\right) \times a_w(\lambda_{NIR}) \times \rho_w(\lambda_{NIR}),$$

$$\text{With } w = \frac{\lambda_2 - \lambda_3}{\lambda_1 - \lambda_3}, \tag{4}$$

In eq. (4), $\lambda_1 = 470$ nm, $\lambda_2 = 482.5$ nm, $\lambda_3 = 490$ nm, $\lambda_{NIR} = 700$ nm and the water absorption at 700 nm, $a_w(\lambda_{NIR}) = 0.57$ m^{-1} (Kou et al., 1993).

The MALH, which represents an absorption anomaly at 482.5 nm, will be positive for *P. globosa* dominated waters and negative or close to zero when *P. globosa* is at low or negligible concentration.

In view of the uncertainties in accurately estimating this 482.5 nm absorption anomaly, it is proposed here to reduce the continuous MALH to a yes/no/unknown flag, similar to the LI yes/no flag. This would be quite appropriate for end-users who would use a chlorophyll-a estimate as proxy for biomass and be quite satisfied with a yes/no flag indicating *P. globosa* dominance in the case of high biomass blooms. Then, MALH has been related to LI and transformed to a qualitative index with a logistic regression. Logistic regression is a generalized linear model regression with a logit transfer function. It allows to obtain from MALH an estimation of the probability (p) that *P. globosa* is the dominant

species according to LI. The obtained logistic regression model (Fig. 2) was found to be significant ($p_{value} < 10^{-16}$ for intercept and slope) and p could be estimated with the following equation.

$$p = \frac{e^y}{1+e^y} \; with \; y = 608.4 \; MALH - 3.84 \quad (5)$$

From this model, the MALH values corresponding to $p = 0.1$ (MALH = 0.003) and $p = 0.9$ (MALH = 0.010) were used as thresholds and interpreted such as

- MALH >0.010 m^{-1} indicates a high biomass *P. globosa* bloom
- MALH <0.003 m^{-1} indicates absence of *P. globosa*
- 0.003 m^{-1} > MALH >0.010 m^{-1} is considered uncertain

Finally, as our main objective is the detection of high *P. globosa* biomass, LI and MALH were calculated only if the chlorophyll-a concentration ([Chl-a] hereafter) associated to the reflectance spectra was higher than 10 mg m^{-3} [Chl-a] has been calculated from reflectance spectra using the hyperspectral algorithm proposed by Ruddick et al. (2001). This algorithm is an improvement of the NIR-red band ratio algorithm developed by Gons (1999) for high [Chl-a] since it avoids the calculation of NIR backscattering. The 10 mg m^{-3} threshold limits attention to the high biomass blooms which are close to the OSPAR "eutrophication problem" threshold of 15 mg m^{-3} (Van der Zande et al., 2019b). In addition, at lower concentrations even [Chl-a] retrieval has high uncertainty here (Ruddick et al., 2001).

2.3. Simulation of satellite measurement errors

To simulate radiometric data from a satellite-based sensor, different sources of error in the water reflectance have been considered. The simulated sources of error include the potential problem of a) inter-band calibration accuracy as they can be highly problematic for second derivative calculation (Stumpf and Werdell, 2010), b) error in atmospheric correction and finally c) radiometric noise. These uncertainties were then added to the measured PANTHYR water reflectance to simulate water reflectance retrieved from a satellite sensor (Eq. 6).

$$\rho_{w_{SAT}}(\lambda_i) = \rho_{wm}(\lambda_i) + \Delta\rho_{RCAL}(\lambda_i)/T + \Delta\rho_{AC}(\lambda_i) + \Delta\rho_{RN}(\lambda_i)/T \quad (6)$$

In eq. 6, T is the downward and upward total transmittance and $\Delta\rho_{RCAL}(\lambda_i)$, $\Delta\rho_{AC}(\lambda_i)$ and $\Delta\rho_{RN}(\lambda_i)$ are errors in reflectance units derived from respectively artefacts in inter-band relative calibration, atmospheric correction errors and radiometric noise. Their calculation is explained in the following sections (i.e. 2.3.1, 2.3.2 and 2.3.3). The impact of these different sources of error are tested individually and together (Section 3.2). For testing, LI and MALH are recalculated after adding uncertainty sources and the conclusion on the absence versus dominance of *P. globosa* is compared to what was obtained from the same in situ water reflectance spectra without additional uncertainty. Then, the proportion of correct retrieval is analyzed (Section 3.2).

2.3.1. Simulation of inter-band relative calibration errors

As calibration factors (i.e. gains to convert digital numbers recorded by a photodetector to radiance in SI units) are multiplicative, $\Delta\rho_{RCAL}(\lambda_i)$ is defined as the factor of the top of atmosphere (TOA) reflectance signal and a gain coefficient dependent on wavelength (Eq. 7). For each spectral band λ_i, $x(\lambda_i)$ is generated randomly from a uniform probability distribution with known standard deviation (E). Here E can be interpreted as an average percentage of error. Finally, TOA reflectance is defined as the addition of atmospheric reflectance (ρ_{atm}) simulated with the 6SV radiative transfer model (Wilson, 2013) and water reflectance derived from in situ PANTHYR measurements (Eq. 8).

$$\Delta\rho_{RCAL}(\lambda_i) = \rho^{TOA}(\lambda_i)\, x(\lambda_i), with \; x(\lambda_i) \in U\left[-\sqrt{3}\;E, \sqrt{3}\;E\right] \quad (7)$$

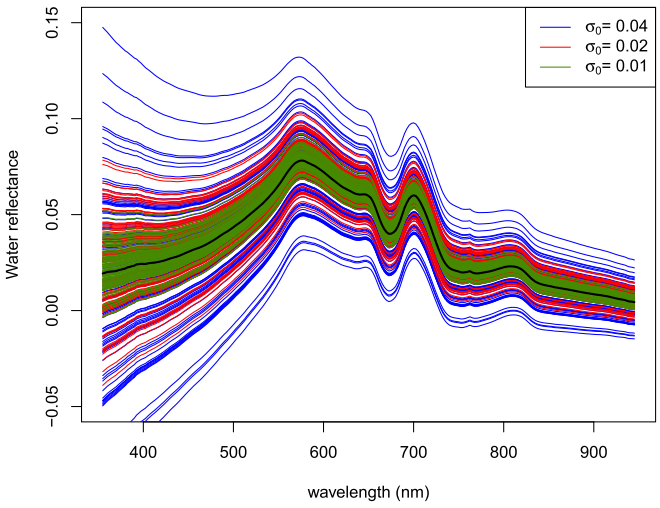

Fig. 3. 100 simulated $\rho_{wm} + \Delta\rho_{AC}$ (blue, green and red lines) for a unique ρ_{wm} (black line) from 2020/08/10.

$$\rho^{TOA}(\lambda_i) = \rho_{atm}(\lambda_i) + T\rho_{wm}(\lambda_i) \quad (8)$$

6SV simulations were performed with a fully absorbing ocean with a wind speed of 5 m s^{-1}, a maritime aerosol model with aerosol optical thickness at 550 nm of 0.1. View zenith and azimuth angles were respectively set to 36° and 180° in order to reproduce the geometry of the CHRIS-PROBA hyperspectral sensor for Ostend images (Lavigne et al., 2021) and solar zenith angle was defined by the position of the target and the date and time of measurements. To represent the most probable period of satellite overpass, only PANTHYR measurements collected between 10:00 and 14:00 UTC were retained and only clear sky condition spectra were selected in the quality control applied to PANTHYR radiometric data (see Section 2.2.1). Then, solar zenith angle was rounded to the closest value on a 5°-step sequence because, to limit calculation time, simulations were performed for solar zenith angles ranging from 25° to 55° by steps of 5°.

Water reflectance time-series with additional inter-band calibration errors were thus produced. Within each time-series, the vector $x(\lambda_i)$ is constant as it is assumed that calibration error is quite stable over time. To analyze the potential impact of inter-band calibration, 100 simulations were made with different randomly generated vectors $x(\lambda_i)$.

2.3.2. Simulation of atmospheric correction error

Errors in atmospheric correction $\Delta\rho_{AC}$ have been represented by an inverse power law model (eq. 9) following the spectral shape of the atmospheric reflectance signal. Indeed, atmospheric correction error generally results from an imperfect estimation of aerosol path reflectance leading to higher extrapolated errors in the blue spectral bands than in red or NIR. This have been verified by Vanhellemont and Ruddick, (2021, Fig. 9) which shows the comparison of in situ PANTHYR measurements at Ostend RT1 station with Sentinel 3 OLCI data.

$$\Delta\rho_{AC}(\lambda_i) = \Delta\rho_0 \left(\frac{400nm}{\lambda_i}\right)^{1.8} \quad (9)$$

In eq. 9, the coefficient 1.8 has been chosen to fit the RMSD ACOLITE curve in Vanhellemont et al. (2021, Fig. 9). The ACOLITE Dark Spectrum Fitting algorithm is considering to be a promising approach for hyperspectral atmospheric correction (i.e. CHRIS-PROBA Lavigne et al., 2021) because it may benefit from extra spectral bands. Importantly in the context of phytoplankton species applications, it avoids assumptions on the water inherent optical properties and is thus not biased to any particular phytoplankton absorption spectra. $\Delta\rho_0$ was randomly generated from a Gaussian distribution of mean 0 and standard deviation σ_0.

Table 1
Target radiance observed in CHRIS-PROBA Ostend images in spring (L) and SNR values used to test impact of radiometric noise of *P. globosa* retrieval.

Wavelength (nm)	L ($W\ m^{-2}\ \mu m^{-1}\ sr^{-1}$)	SNR Level 1	SNR Level 2	SNR Level 3
470	63	200	400	1000
482.5	59	200	400	1000
490	55	200	400	1000
700	15	130	250	600

Finally, 100 simulations of water reflectance time-series are performed for each of 3 σ_0 values set to 0.01, 0.02 and 0.04. Among these values, 0.02 is the one which best fits Vanhellemont et al. (2021) results. Contrary to $\Delta\rho_{RCAL}$, $\Delta\rho_{AC}$ values are different and independent for each observation as it can be assumed that atmospheric correction error is independent from one image to the other. Fig. 3 shows the 100 simulations of atmospheric correction error for one reflectance spectrum of the PANTHYR time-series.

2.3.3. Simulations of radiometric noise

Another potential source of error to consider in satellite-derived water reflectance measurements is the radiometric noise. Radiometric noise is random and is characterized for each instrument by the signal to noise ratio (SNR hereafter). From SNR, the noise equivalent reflectance (ρ_{NE}) which represents the level of noise in reflectance units can be calculated with the following equation

$$\rho_{NE} = \frac{\pi \frac{L}{SNR} d^2}{F_0 cos\theta_s} \tag{10}$$

where F_0 is the extra-terrestrial solar irradiance, d is sun-earth distance in Astronomical Units ($d \approx 1$), θ_s is the solar zenith angle and L is the typical TOA radiance expected in spring and summer in the BCZ. L values have been estimated from images of the hyperspectral CHRIS-PROBA sensor at RT1 station (Table 1) and θ_s is defined by the date and time of measurements in the PANTHYR time-series. Different SNR values have been tested (see Table 1) to represent different sensor's performances. Finally, the radiometric noise ($\Delta\rho_{RAD}$) has been simulated by random number generation from a uniform probability distribution of mean 0 and standard deviation ρ_{NE} similarly to Lavigne and Ruddick (2018) and has been added to the PANTHYR water reflectance.

3. Results

3.1. Detection of P. globosa from above water radiometry

3.1.1. Algorithm validation using the cruise data

When testing ALH and MALH against in situ observations, both algorithms show similar and positive results in presence of *P. globosa* (relative abundance ≥ 0.05) with MALH and ALH higher than 0.003, the uncertain threshold. The presence of *P. globosa* was also well detected by the LI algorithm. The main differences are observed in the absence of *P. globosa*. Whereas MALH shows negative values ranging from −0.005 to 0, ALH shows for most of those points values close to 0, but one datapoint (blue point on Fig. 4A and B) shows MALH = −0.0053 whereas ALH = 0.0063, indicating a (erroneous) ALH suspicion of *P. globosa*. For the blue and green points on Fig. 4, one can notice very different second derivative spectra for quite similar ALH values (ALH = 0.0063 blue point, ALH = 0.0082 green point). The red and green curves that correspond to the presence of *P. globosa* show a maximum around 475 nm whereas the maximum is around 465 nm for the blue curve (Fig. 4C). Second derivative minima are also shifted; there is a minimum around 485 nm in the blue curve and around 510 nm in the red and green curves. These observations, although based on a small number of observations, validate the Lubac et al. (2008) and MALH algorithms but suggest that the ALH algorithm, which focuses on the 450 nm – 480 nm region of the spectra, is erroneous.

3.1.2. Spring bloom monitoring at RT1 station

Temporal evolution of [Chl-a] and *P. globosa* indexes are represented in Fig. 5 for the spring and summer 2020. A strong spring bloom is observed from 2020-04-15 to 2020-05-15 with [Chl-a] concentrations ranging from 20 to 60 mg m^{-3}. Then, [Chl-a] reaches background values lower than 20 mg m^{-3}, except during a very short event marked by [Chl-a] up to 60 mg m^{-3} in late June. The general time-series marked by an April–May increase of [Chl-a] is consistent with previous observations in the Belgian coastal waters (Gypens et al., 2007). The analysis of *P. globosa* indexes MALH and LI (panel B) shows consistent results with a detection of *P. globosa* dominance from LI when MALH is high. Both indexes reveal a unique and short period of *P. globosa* bloom lasting from end of April to early May. Results also show clear discrepancies between the original Astoreca et al. (2009) index (ALH, Fig. 5C) and the newly introduced modified version (MALH, Fig. 5B). Main differences are observed by end of June when [Chl-a] sharply increases, MALH shows strong negative values whereas ALH shows strong positive values. Whereas it is clear that the intensity of each index is correlated with [Chl-a], ALH indicates the presence of *P. globosa* whereas MALH in

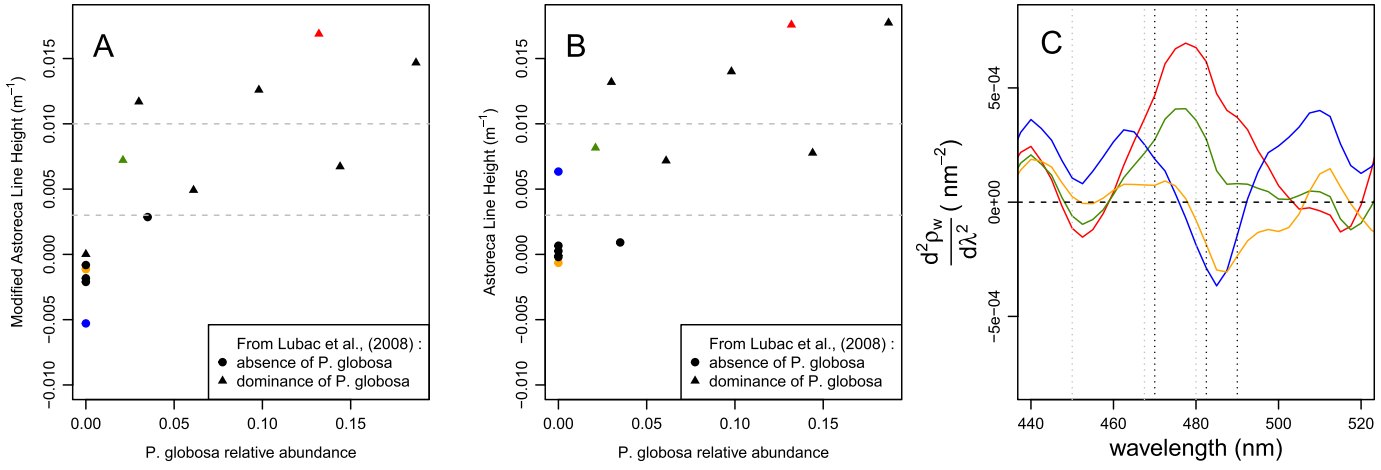

Fig. 4. MALH and ALH versus in situ measurements of *P. globosa* (from DNA barcoding), panels A and B respectively. Shape of the points indicates the result of LI algorithm. Panel C: second derivative spectra for selected data points (see colors on panels A and B).

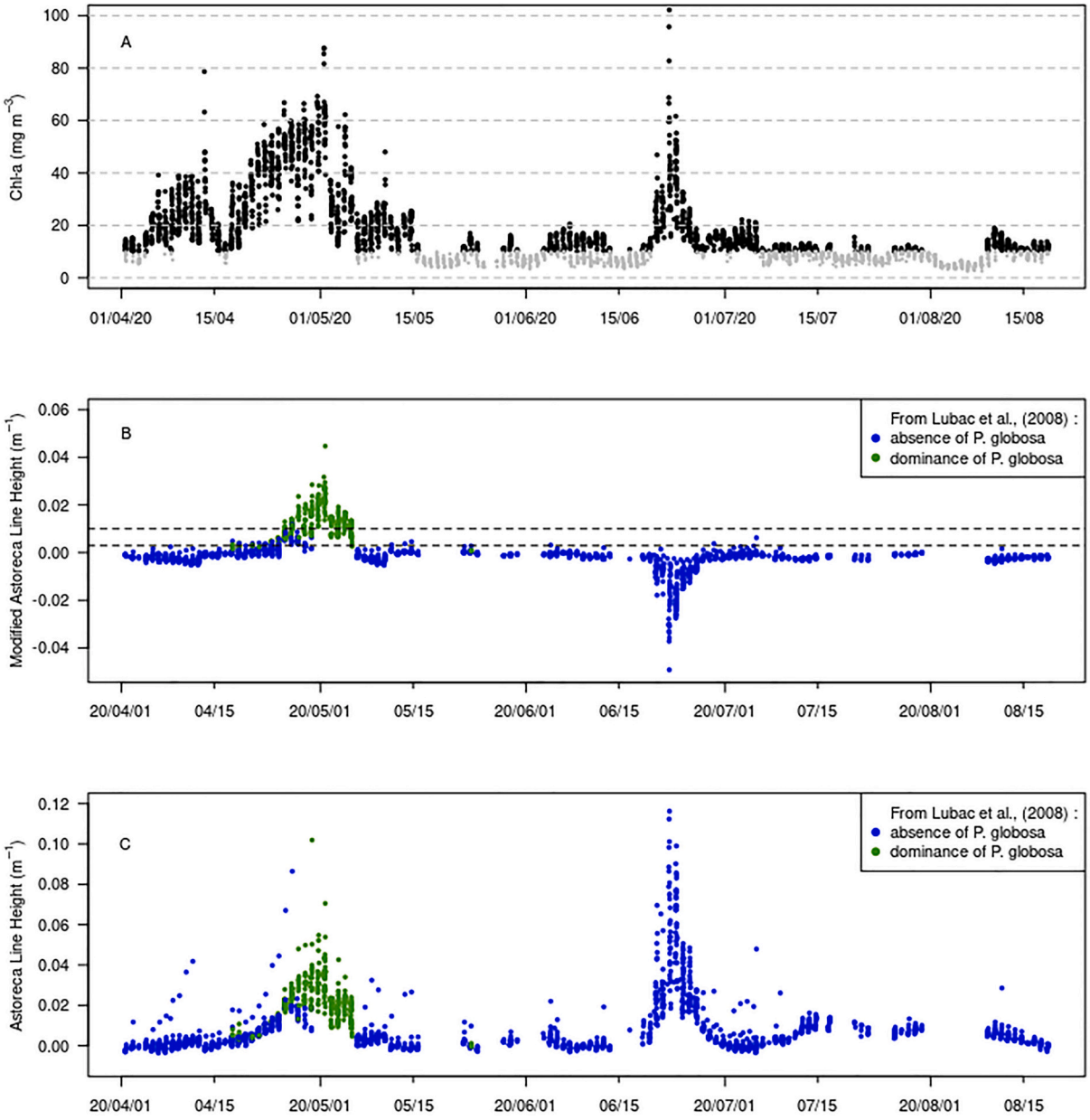

Fig. 5. Time-series of [Chl-a] concentration estimated from water reflectance measurements at RT1 station (panel A). Because of limitations of the NIR-red band ratio [Chl-a] algorithm, estimations <10 mg m^{-3} which have been removed from the *P. globosa* detection analysis are in grey. Time-series of Modified Astoreca Line Height (MALH, panel B) and original Astoreca Line Height (ALH, panel C). MALH and ALH differ by the selection of wavelengths used in the algorithms (450–467.5-480 nm and 470–482.5-490 nm for ALH and MALH respectively). Colors show the outcome of the Lubac et al. (2008) index for *P. globosa* dominance. Horizontal dotted lines (panel B) indicate the upper and lower MALH thresholds for absence and dominance of *P. globosa* respectively. (For interpretation of the references to colour in this figure legend, the reader is referred to the web version of this article.)

agreement with LI indicating the absence of *P. globosa.* This discrepancy between ALH and MALH is similar to the observations made on Fig. 4 for the blue point: whereas ALH is positive, MALH is negative in agreement with LI indicates the absence of *P. globosa*. In Fig. 4, MALH and LI are validated with in situ observations which confirm the absence of *P. globosa*. This last result also agrees with recent findings of Castagna et al., 2021 which have shown that ALH is not really correlated with Chl-c_3 but rather to total Chl-*c* and hence would increase with total phytoplankton biomass. In addition, LI and MALH are consistent with previous observations showing that in the Belgium coastal zone the spring phytoplankton bloom is dominated successively by diatoms, *P. globosa* and diatoms again but with lower concentrations (Breton et al., 2006; Lancelot et al., 2005; Gypens et al., 2007). Indeed, while no systematic phytoplankton measurements were made in 2020, measurements from previous years suggest that *P. globosa* should be detected in April–May and not in June–September. The phytoplankton measurements carried out by (Muylaert et al., 2006; Fig. 6) in nearby waters in 2003 show presence of *P. globosa* in April and in some locations March, but absence at all stations for June–September. The phytoplankton measurements carried out at least twice a month from 1988 to 2000 (Breton et al., 2006; Fig. 2) at a location 40 km further offshore show a *P. globosa* bloom every year in March/April/May and negligible *P. globosa* colony biomass for June–September (see climatology, Fig. 6). Diatom blooms are found at various moments during the period March–September with significant interannual variability of intensity and timing. The temporal succession of diatoms and *P. globosa* blooms is explained by unbalanced nutrient supply as *P. globosa* grows when diatom growth is limited by silicate and inorganic phosphate (Breton et al., 2006; Lancelot et al.,

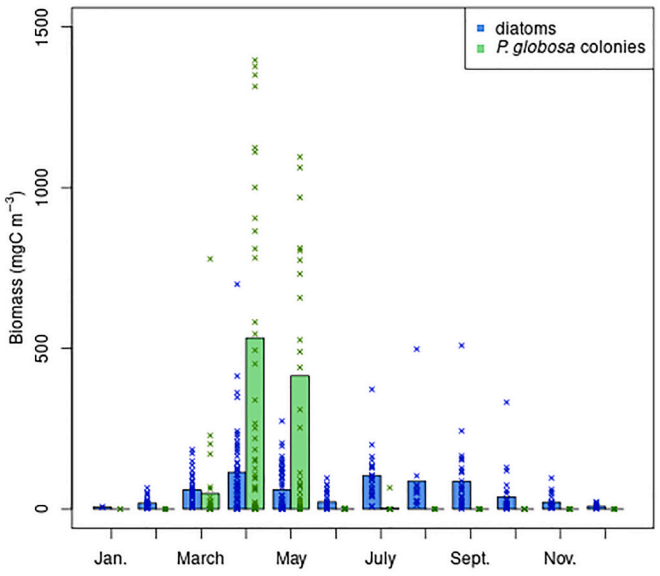

Fig. 6. Monthly climatology of diatoms and *P. globosa* carbon biomass in Belgian waters. Colour bars show monthly multi-year means and the "x" symbols refer to each individual measurement. This climatology has been produced from data collected between 1988 and 2000 in Belgium waters at location 40 km further offshore the RT1 platform. The dataset is presented by Rousseau (2000).

2005; Lacroix et al., 2007; Blauw et al., 2010). Therefore, we expect *P. globosa* to be present in March–May and absent in June–September.

The analysis of the second derivative was performed for some key dates during the spring/summer season (Fig. 7) and all along the *P. globosa* bloom development (Fig. 8). Fig. 7 shows reflectance spectra and second derivative during the pre and post *P. globosa* bloom (2020-04-10 and 2020-05-10) where [Chl-a] was respectively 23 mg m^{-3} and 27 mg m^{-3}, during the *P. globosa* bloom (2020-05-01, [Chl-a] = 87 mg m^{-3}) and during the short and intensive bloom that occurred in June (2020-06-22, [Chl-a] = 96 mg m^{-3}). Results (Fig. 7, panel A) show large differences in overall magnitude relating to backscatter from non-algae particles. The impact of high [Chl-a] absorption can also be seen in the range 650–710 nm for all these spectra. While only small differences in reflectance spectra (Fig. 7A) can be observed with relevance to pigments which may differ between species, it is still possible to observe divergences in concavity and convexity when focusing on the region of interest (Fig. 7B). These divergences are emphasised by the second derivative analysis. Indeed, the spectrum for 2020-05-01 (Fig. 7, panel C) which represents the *P. globosa* bloom shows a contrasted pattern. Whereas other curves show a second derivative maximum around 465 nm, *P. globosa* second derivative maximum is shifted to 475 nm. Around 510 nm large difference between *P. globosa* spectra (2020-05-01 curve Fig. 7C) and other spectra are also observed. A negative minimum is observed for *P. globosa* and a maximum with positive values for other spectra. All these observations are consistent with the results of Lubac et al. (2008) and with the dataset of in situ observations (Fig. 4). The shifted maximum in *P. globosa* was explained by the presence of Chl-c_3 which is a biomarker of *P. globosa* in the North Sea (Breton et al., 2000; Astoreca et al., 2009) and has an absorption peak slightly shifted compared to Chl-c_1 and Chl-c_2. After extraction in solvent, Chl-c_1, Chl-c_2 and Chl-c_3 absorption peaks were observed around 446 nm, 449 nm and 452 nm respectively by Zapata et al. (2006) and total Chl-*c* absorption maximum was observed around 460 nm in vivo by Bidigare et al. (1990) and by Hoepffner and Sathyendranath (1991). The divergences around 510 nm were explained by a lower concentration in carotenoids in *P. globosa* compared to other diatoms species observed in the North Sea (Lubac et al., 2008; Castagna et al., 2021). The analysis of the second derivative (Figs. 4C, 7C and 8) demonstrates well the need to modify wavelength selection in Astoreca et al. (2009) algorithm. Indeed, all the interactions between pigments need to be considered and new shifted wavelengths (i.e. 470 nm – 482.5 nm – 490 nm) seem to better capture *P. globosa* pigment specificity.

The very high temporal resolution of reflectance time-series acquired with the PANTHYR system allows to observe from the second derivative the evolution of the *P. globosa* bloom from onset to decay (Fig. 8). From 2020-04-20 to 2020-05-02, a progressive shift from ~465 nm to ~475 nm in the position of the second derivative maximum is clearly observed as well as the progressive disappearance of the second derivative minimum around 485 nm. However, between the 4th and the 6th of May a sudden curve inversion appeared and from the 6th of May the second derivative is similar to what is observed before the 20th of April, the situation before *P. globosa* bloom onset. These results suggest that

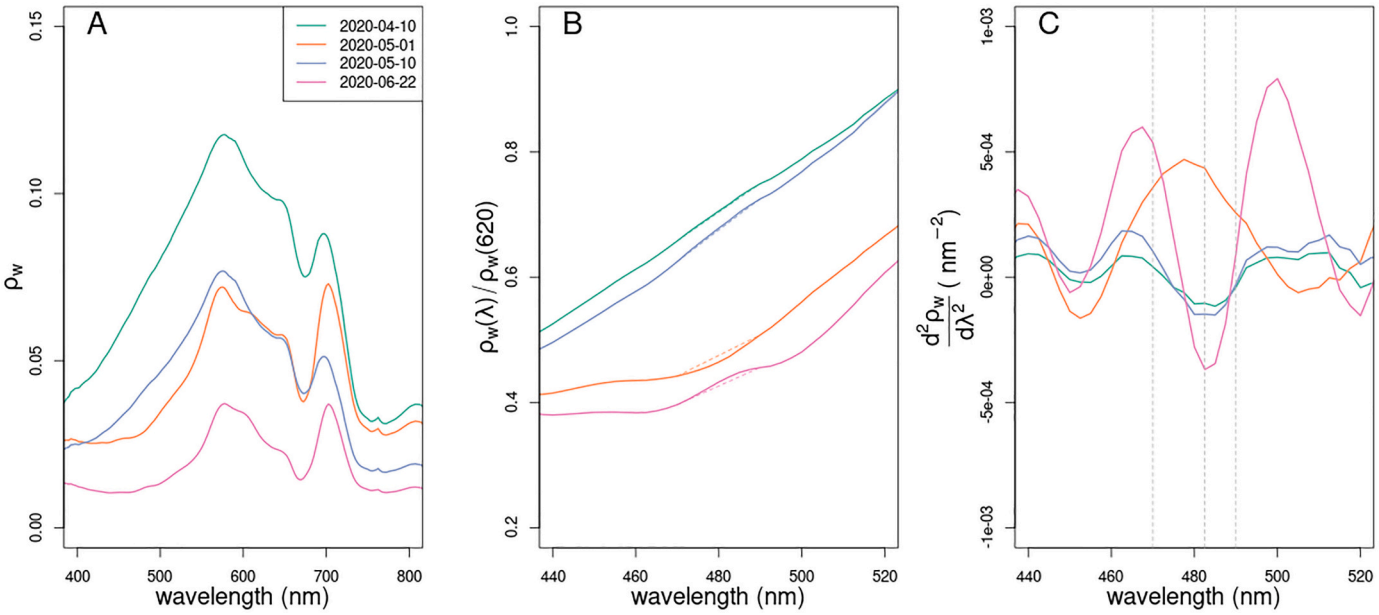

Fig. 7. Four selected spectra of water reflectance (panel A), 620 nm-normalized water reflectance with a zoom in the 440 nm - 520 nm spectral range (panel B). Dashed lines highlight the extra absorption attributed to *P. globosa*. Panel C shows the second derivative of reflectance spectra in the spectral range 440 nm - 520 nm.

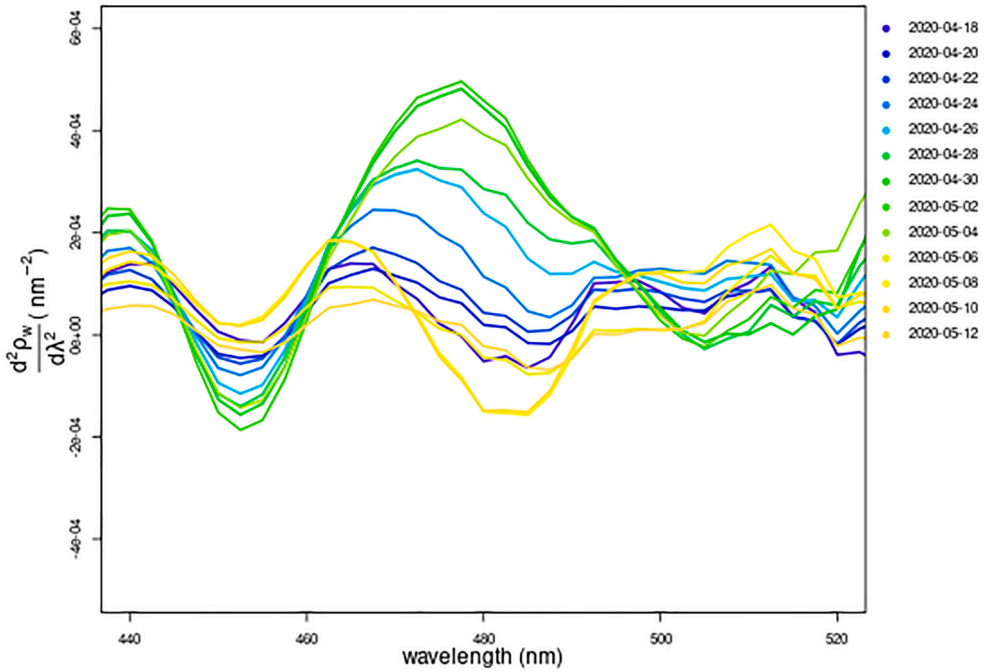

Fig. 8. Evolution of the second derivative of the reflectance spectra during the period 2020/04/16–2020/05/12 at 13:00 UTC.

P. globosa progressively increases up to reaching a period of maximum concentration (2020-04-30 to 2020-05-02) before sudden collapse. This is consistent with previous findings which attribute *P. globosa* decay to nitrate and organic phosphate depletion (Gypens et al., 2007; Blauw et al., 2010), but is observed here in unprecedented temporal resolution thanks to the reflectance dataset.

3.2. Impact of satellite measurement errors

Fig. 9 shows the impact of inter-band calibration errors on the detection of *P. globosa* with both LI and MALH algorithms. Results indicate that both algorithms are extremely sensitive to inter-band calibration. As expected, when E increases, the rate of false positive and false negative increases in both algorithms. LI and MALH algorithms show similar results with a correct retrieval of *P. globosa* status for E = 0.1%. With the "uncertain" condition of the MALH algorithm (blue bars), the rate of false negative and false positive is lower than with the LI algorithm for small inter-band uncertainty rate (E = 0.1%, E = 0.5%). This "uncertain" status is important as it avoids misinterpretation of the results. In both algorithms, the risk of false negative is higher than the risk of false positive. In the Lubac et al. (2008) algorithm, this is explained by the definition of the algorithm. Indeed, the probability to encounter in the 480–499 nm range (20 nm width) a random negative peak, resulting from high inter-band uncertainty and interpreted as an absence of *P. globosa* is higher than in the 500–510 nm range (10 nm width). The risk of false negative becomes very significant (30 to 40%) when E reaches 0.5% indicating that none of the algorithms are suitable in such conditions. Fig. 10 shows that with MALH good retrieval of *P. globosa* absence or dominance is sensitive to the MALH value with lower performance for MALH between 0 and 0.01 m^{-1} whereas with LI index good retrieval of *P. globosa* dominance is insensitive to the MALH value. This last result means that the shape of the second derivative spectra has no influence on LI performance and only the E value is impacting. This makes sense as any random peak in the second derivative can affect LI algorithm and E determines the intensity of random perturbations on the second derivative spectra.

Finally, these results suggest that with both LI and MALH algorithms a very good (E = 0.1%) relative inter-band calibration is necessary to retrieve *P. globosa*. With E = 0.25%, the MALH algorithm seem to be more appropriate as the risk of false negative and positive is limited to 15% and 5% respectively thanks to the "uncertain" condition. With LI algorithm this risk is slightly higher (about 25% and 20%).

As shown by Fig. 11, the impact of error on atmospheric correction is much less problematic than inter-band calibration error for both LI and MALH indexes. LI shows the best results with high rates of correct detection of *P. globosa* dominance (values ranging between 85% and 100%) and *P. globosa* absence (values higher than 90%). Although rates of correct *P. globosa* dominance detection are a bit lower with MALH (from 85% to 65%) than with LI, the rate of false negative with MALH remains very low (<10%) indicating that most of the time, when *P. globosa* is not detected the conclusion is "uncertain" rather than the absence of *P. globosa*. Then, even if uncertainty slightly increases, both MALH and LI indexes seem to be robust to potential error in atmospheric correction. Better performance of LI when introducing atmospheric correction error (Fig. 11) confirms that LI is more sensitive to spectrally random noise and less sensitive to spectrally coherent errors of atmospheric correction. In the 460–510 nm range where second derivative is calculated in the LI algorithm, the second derivative of $\Delta\rho_{AC}(\lambda)$ is almost linear with a small variability range (about 3.10^{-7} for $\Delta\lambda_0$ equals 0.04, see eq. 9 for $\Delta\rho_{AC}(\lambda)$ and $\Delta\lambda_0$ definitions) which explains its minimum impact on the second derivative of $\rho_m(\lambda) + \Delta\rho_{AC}(\lambda)$ and on *P. globosa* retrieval.

Fig. 12 shows the impact of radiometric noise on *P. globosa* detection with MALH. For sensors with lower radiometric performance such as sensors primarily dedicated to terrestrial applications, at native spatial resolution, radiometric noise significantly hinders *P. globosa* retrieval with a rate of false negative of about 40% and 25% for SNR level 1 and SNR level 2 respectively. However, radiometric noise can be reduced by degrading spatial resolution and averaging several pixels. Averaging 81 pixels (9 × 9 pixels side box) significantly reduces the impact on MALH and allows to avoid a wrong detection of *P. globosa* absence or dominance from the two examples shown in Fig. 12. However, in case of low SNR (SNR level 1) to improve even more the estimation of high MALH values, it is necessary to average even >81 pixels. Hence, these result show that as soon as pixels can be averaged the radiometric noise does not prevent the remote sensing detection of. *P globosa* bloom. Indeed,

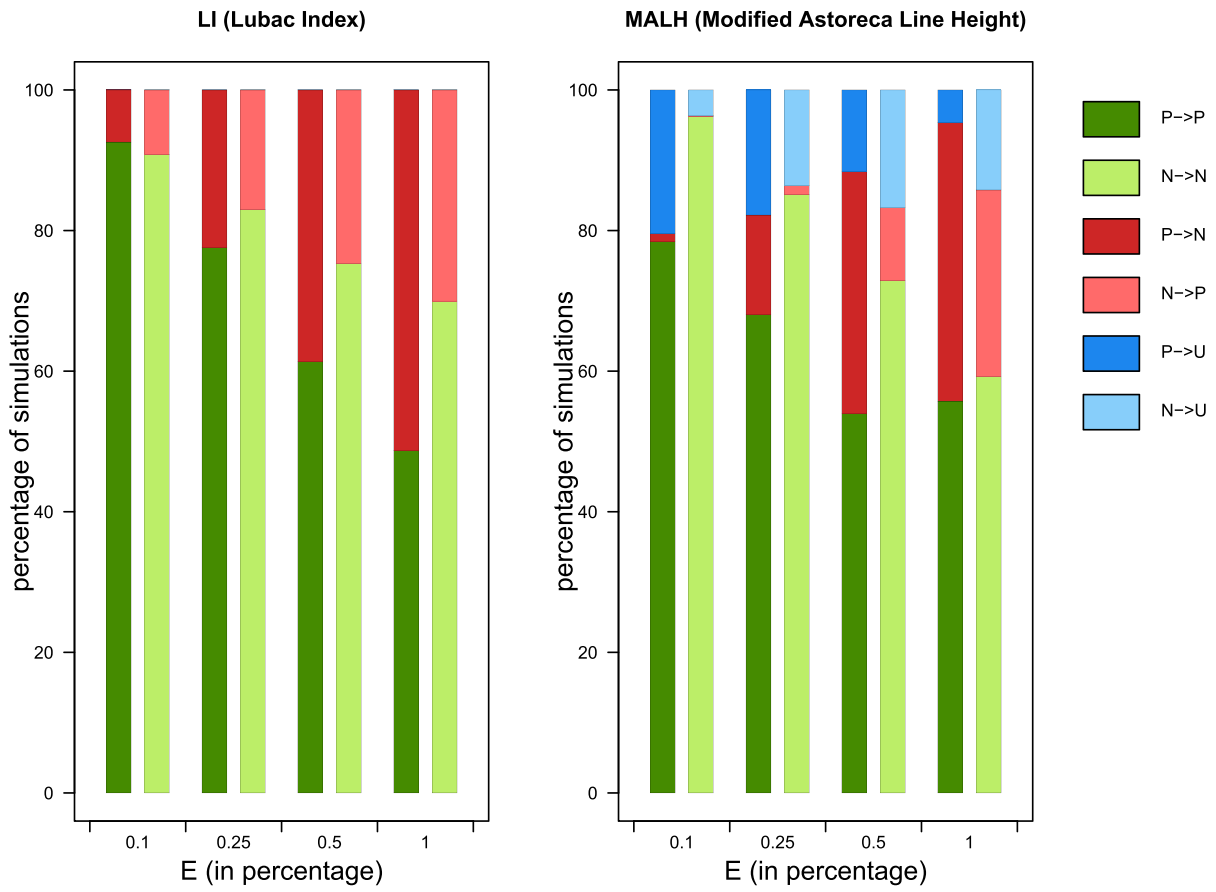

Fig. 9. Percentage of good (green bars) and bad (red bars) retrieval after application of inter-band calibration error disturbance. E is the average percentage of error on inter-band calibration (see eq. 7 for definition). "P- > P" and "N- > N" refers to a correct detection of *P. globosa* dominance (P: Positive) and absence (N: Negative) respectively. "P- > N" and "N- > P" refers to an erroneous detection of *P. globosa* dominance (false negative) and absence (false positive) respectively. For MALH algorithm only, "P- > U" and "N- > U" are used when uncertain MALH value is retrieved. Dark and light colour bars represent the distribution of simulations for initial data points of PANTYR reflectance time-series identified as *P. globosa* "positive" (dominance) and "negative" (absence) respectively. (For interpretation of the references to colour in this figure legend, the reader is referred to the web version of this article.)

since the absence/dominance of *P. globosa* is expected to occur over larger horizontal length scales than phytoplankton biomass, a reasonable monitoring strategy would be to estimate [Chl-a] at the highest spatial resolution and *P. globosa* absence/dominance at a lower spatial resolution.

Finally, the simulated errors in inter-band relative calibration, atmospheric correction and radiometric noise have been combined to simulate an ocean colour satellite sensor. For inter-band relative calibration, E has been set to 0.1% and 0.25% at top of atmosphere, the medium error model of atmospheric correction error has been chosen ($\sigma_0 = 0.02$) and for radiometric noise the SNR level 2 has been selected with an averaging over 9×9 pixels. Simulations were performed with MALH. Fig. 13 shows results of *P. globosa* detection from the PANTHYR data (upper line) and from 100 simulations. The absence of *P. globosa* is generally well detected in >90% of simulations when E = 0.1% and about 80% when E = 0.25%. In simulations, the dominance of *P. globosa* is detected in 50% to 80% of simulations according to the *P. globosa* bloom intensity when E = 0.1% and from 50% to 60% when E = 0.25%. These results confirm that *P. globosa* detection from remote sensors can only be achieved with strong requirements on the sensor inter-band calibration and with compromises on spatial resolution when needed. They are discussed in Section 4.2.

4. Discussion and conclusion

4.1. Radiometric monitoring of P. globosa bloom

The present results demonstrate for the first time the potential of autonomous above water radiometric measurements for the monitoring of *P. globosa* in the North Sea. Indeed, autonomous above water radiometers whose primary objective is to validate satellite data of remote sensing reflectance (Goyens et al., 2018) could have additional applications in phytoplankton group monitoring. Present results are based on existing algorithms (Lubac et al., 2008; Astoreca et al., 2009) originally developed from a limited number of shipborne reflectance measurements but tested here with a full 5-month time series at high temporal resolution.

P. globosa monitoring in the Southern North Sea is mostly based on regular in situ samples (Lancelot et al., 1987; Mills et al., 1994) and some autonomous measurements based on flow cytometry (Bonato et al., 2016) and spectrofluorometry (Houliez et al., 2012) which are however often dependent on oceanographic vessels. In this framework, autonomous hyperspectral radiometers should help to complete *P. globosa* monitoring by providing additional information for some fixed stations but at a very high temporal resolution adapted to the rapid evolution of *P. globosa* bloom. In the future, it would be ideal to operate autonomous flow cytometers (Sosik and Olson, 2007) in parallel with autonomous hyperspectral radiometric measurements, as recommended by Dierssen et al. (2020). Indeed, autonomous detection of

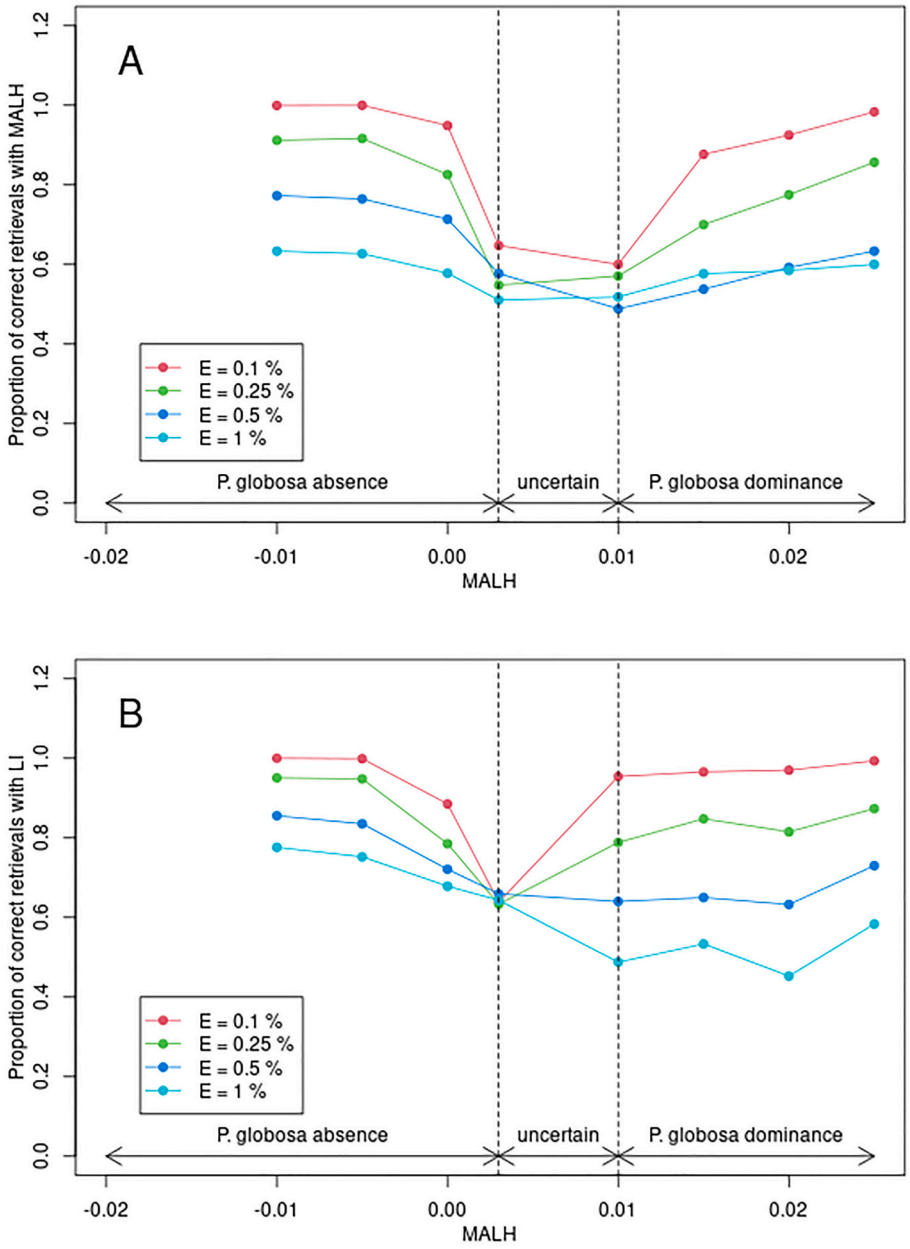

Fig. 10. Proportion of correct absence/dominance *P. globosa* retrieval as a function of the MALH value after simulation of the inter-band calibration error disturbance. Colors refers to the level of error (E) as defined in Section 2.3.1.

phytoplankton cells by flow cytometers would allow for an improved validation of radiometric based algorithms, determining whether other phytoplankton species with the same pigment signature as *P. globosa* could interfere with *P. globosa* retrieval (Castagna et al., 2021). In addition, it would provide a better understanding of *P. globosa* indexes in terms of concentration of cells per liter. In the present study, the validity of the indexes is based on a limited number of water reflectance / *P. globosa* abundance matchups (Section 3.1.1), on previous results (Lubac et al., 2007; Astoreca et al., 2009) and on our strong general knowledge of phytoplankton blooms in the Belgian coastal zone (Lancelot et al., 2005; Lacroix et al., 2007; Fig. 5) which confirms a posteriori the validity of the algorithms used only for the BCZ.

Although, the MALH and LI algorithms may still be valid outside the BCZ to detect *P. globosa* as suggested by Li et al. (2021) off Southern China, in this study they have only been validated in BCZ. In different regions with different phytoplankton species, an additional validation is needed as MALH and LI algorithms may fail, especially with false positives. MALH measures a phytoplankton absorption anomaly. The variability of this anomaly will clearly be driven by variability of pigments and hence by phytoplankton species. However, the relationships between absorption and pigments and between pigments and species are complex and different species may produce the same phytoplankton absorption anomaly as *P. globosa*. Therefore, there may be a risk of false positive detections in other regions and the present study claims good performance only for the BCZ.

4.2. Challenges of remote sensing observations

The impact of potential sources of uncertainty related to remote sensing measurements was assessed in section 3.2 by comparing results of *P. globosa* detection algorithms (i.e. LI, MALH) applied to a same reflectance spectrum but with and without additional uncertainty sources. Consequently, in Section 3.2, the denomination “correct” retrieval refers to a reference result from in situ water reflectance and

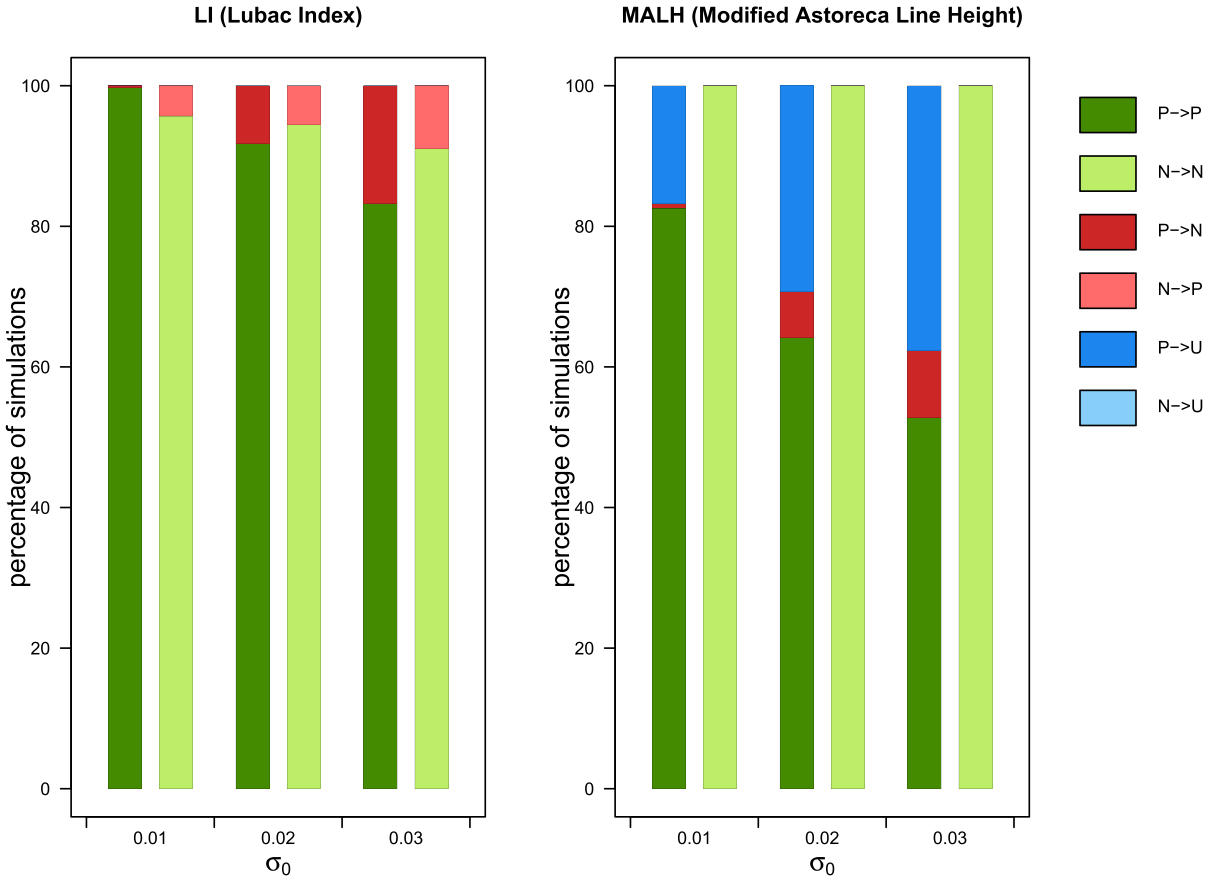

Fig. 11. Percentage of good (green bars) and bad (red bars) retrieval after application of atmospheric correction error. See caption of Fig. 9 for details. (For interpretation of the references to colour in this figure legend, the reader is referred to the web version of this article.)

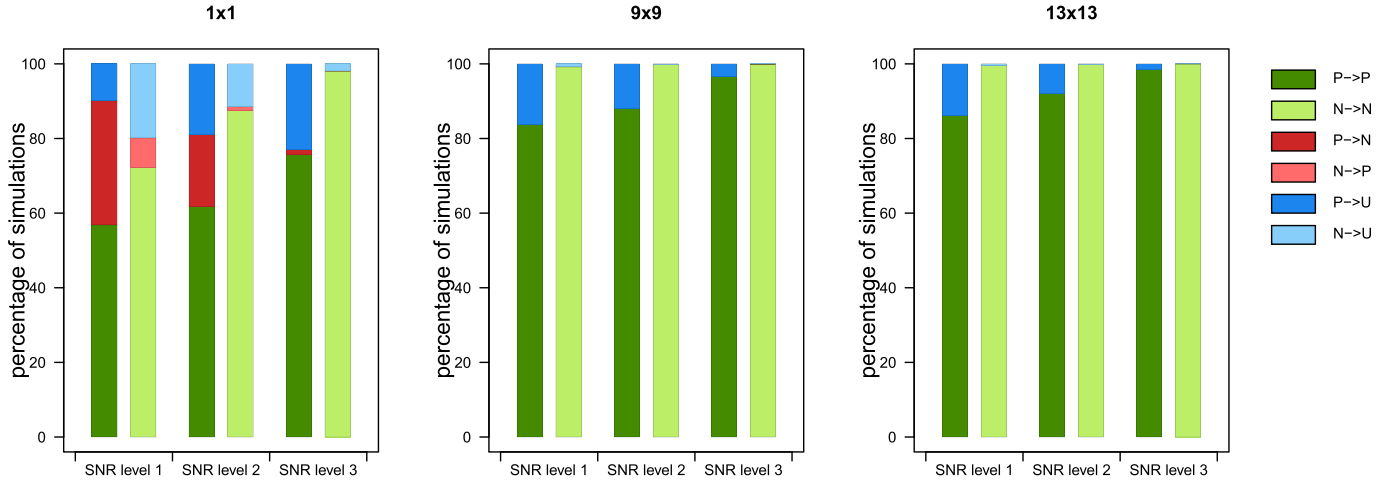

Fig. 12. Percentage of good (green bars) and bad (red bars) retrieval after introduction of radiometric noise with Modified Astoreca Line Height algorithm. SNR level are given in Table 1. Left, middle and right panels test noise reduction after pixel averaging. See caption of Fig. 9 for details. (For interpretation of the references to colour in this figure legend, the reader is referred to the web version of this article.)

not from in situ measurement of phytoplankton cells. Results presented in Section 3.2 show that the detection of *P. globosa* blooms from hyperspectral remote sensing remains challenging. Indeed, as shown on Fig. 7B, the characterization of *P. globosa* bloom relies on the detection of very slight changes in water reflectance spectra. Hence, it requires high spectral resolution but also a very accurate inter-band relative calibration and low radiometric noise. Previously, for typical multispectral ocean colour sensors, 1% uncertainty on water leaving radiance was targeted for inter-band relative calibration (Zibordi et al., 2015). The present results require at least 0.25% error in inter-band relative calibration at top of atmosphere which is equivalent for the RT1 PANTHYR time-series to about 0.7% error on water reflectance. Hence, to apply *P. globosa* algorithm on remote sensing data, inter-band relative calibration has to be improved compared to previous

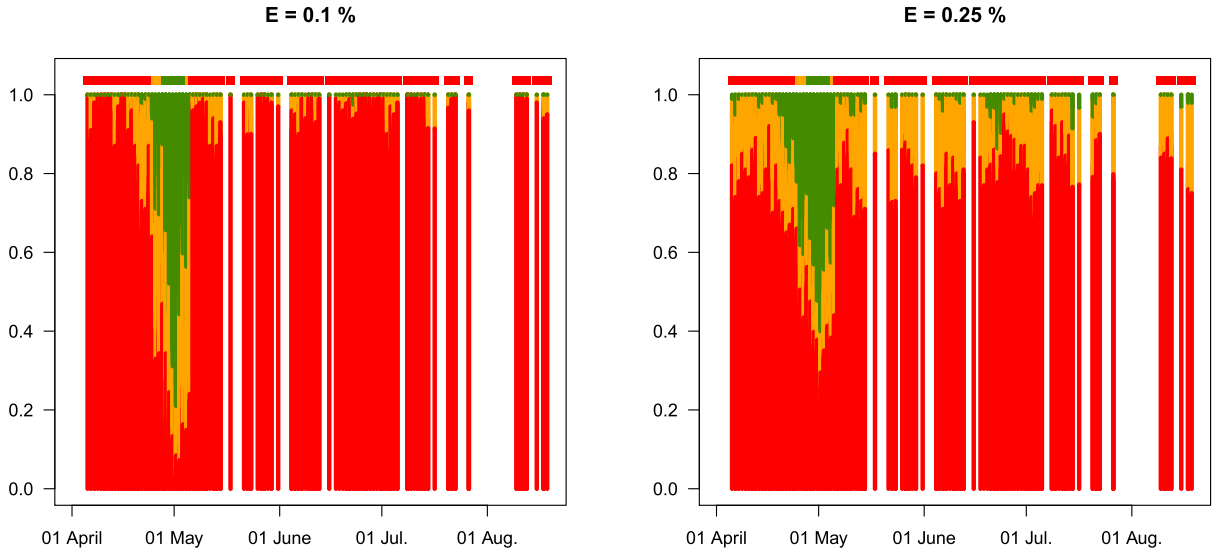

Fig. 13. Barplots representing the proportion of simulations that detected an absence of *P. globosa* (red), a dominance of *P. globosa* (green) or uncertain conditions (MALH between 0.003 and 0.01, orange). Simulation combine the three sources of error set as $\sigma_0 = 0.02$, SNR = level 2 with 9x9pixels averaging and E = 0.1% (left) or E = 0.25% (right). The upper bar shows the *P. globosa* detection from PANTHYR times-series when no error is added, considered as the reference. Only spectra with a [Chl-a] >10 mg m^{-3} are considered which explains the white areas. (For interpretation of the references to colour in this figure legend, the reader is referred to the web version of this article.)

requirements for multi-spectral ocean colour sensors. However, the hyperspectral smoothness of water reflectance spectra and the temporal coherence of radiometric calibration gains should help for the development of vicarious calibration methods dedicated to the improvement of consistency between adjacent spectral bands (Stumpf and Werdell, 2010; Lavigne and Ruddick, 2021; Mizuochi et al., 2020). In particular, Stumpf and Werdell (2010) presented a calibration method based on second derivative comparison particularly adapted to line height difference algorithms like the *P. globosa* algorithm. Given the strong need for vicarious calibration, hyperspectral autonomous radiometer systems such as PANTHYR represent an indispensable in situ data source. Today, the only available remote sensing hyperspectral imagers are CHRIS on PROBA1 for which calibration is not updated anymore and the recently launched PRISMA and DESIS sensors with typically 5% uncertainty at top of the atmosphere (Alonso et al., 2019; Giardino et al., 2020). Hence, without an intensive work on PRISMA or DESIS inter-band relative calibration, it is not possible to detect *P. globosa*. However, for the future PACE mission, the requirement for total calibrated instrument artefact is set to <0.5% (https://pace.oceansciences.org/oci.htm) and one can expect that post processing treatments to improve inter-band calibration will allow the detection of *P. globosa*.

The radiometric noise of satellite sensors can also hinder the detection of *P. globosa* if SNR is too low as is the case with the PRISMA sensor (SNR <160 in visible, Giardino et al., 2020). As demonstrated in this study, it is still possible to degrade spatial resolution to improve SNR but such a compromise prevents the access to short scale spatial variability which might be very important for some particular species and cannot be applied in small lakes. However, with the future PACE-OCI and SBG sensors one can expect largely improved radiometric performances. SNR requirements for SBG is 400 in visible (https://sbg.jpl.nasa.gov/) and >1000 for PACE-OCI (Mannino et al., 2017).

The MALH time-series showed here that the *P. globosa* bloom can be very short (a few weeks), although this may depend on location and inter-annual variability (Blauw et al., 2010). To monitor such a rapid event, the revisit time is very important especially in the North Sea where cloud cover is not negligible. This would favour moderate resolution sensors such as PACE-OCI with a 2-day revisit time compared to high spatial resolution sensors with less frequent coverage. Finally, high spectral resolution is obviously essential (Vandermeulen et al., 2017). In the present study, TriOS radiometer resolution has been used for in situ data analysis (Section 3.1) and satellite error simulations (Section 3.2). Although, radiometric data has been binned at 2.5 nm, initial TriOS sensor sampling interval is 3 nm with a FWHM of 10 nm for each band. As demonstrated by Vandermeulen et al. (2017), the sampling interval is critical to proper resolve water reflectance spectra. From a variogram analysis, authors demonstrated that in the 450 nm – 500 nm range, optimal sampling interval ranges from 4 to 8 nm for different water types. Hence, the short sampling interval of TriOS (i.e. 3 nm) allows to properly capture line height signal position and second derivative patterns whereas a larger sampling interval (e. g. > 10 nm) could lead to significant limitations in the analysis of water reflectance spectra. FWHM also defines spectral sampling features. Large FWHM are generally used to reduce radiometric noise. However, if FWHM is large compared to the spectral scale of the water reflectance signal that need to be observed (here 20 nm), it will tend to smooth it and to reduce its intensity. A coherent signal was still observed in in situ measurements for both LI and MALH algorithms (Section 3.1) which means that although the *P. globosa* signal may be smoothed, the 10 nm FWHM was sufficient. Spectral features of TriOS radiometers are relatively close to the 5 nm spectral resolution of PACE sensor which, as explained above, represents the best opportunity, in a near future, to attempt the monitoring of *P. globosa* bloom from space.

4.3. Conclusion

The results of this study demonstrate that autonomous above water radiometric measurements are able to monitor with an hourly resolution the development of the phytoplankton bloom via [Chl-a] and an indicator of high biomass *P. globosa* blooms in the Belgian Coastal Zone. The high frequency *P. globosa* index data derived from radiometry is particularly relevant for water quality monitoring as *P. globosa* impacts on marine ecosystem and economical activities. However, this data is limited to a fixed station and to be able to routinely monitor the whole North Sea, the feasibility of satellite application of the *P. globosa* algorithms was also tested here.

Although, the present work does not intend to fully simulate a satellite-based water reflectance, the impact of key error sources expected from remote sensing platforms was tested. Results show that

because of their spectral coherence, atmospheric correction errors are not the main issue for *P. globosa* retrieval. Indeed, since they affect each spectral band independently, inaccuracy in inter-band calibration and radiometric noise are much more problematic for the second derivative algorithms used here. Although radiometric noise is expected to be largely improved with the new generation of hyperspectral sensors (e.g. SBG and PACE-OCI) and can be improved by degrading spatial variability, inter-band relative calibration errors appear to be the main limiting factor. Indeed, it was demonstrated that inter-band calibration error should be <0.25% at top of the atmosphere. Such requirements are stronger than current requirements on ocean colour multispectral sensors (1% error of water signal Zibordi et al., 2015) which means that it will be necessary to make use of the hyperspectral resolution to develop a dedicated inter-band vicarious calibration. This work also highlights the need for high temporal resolution (short revisit time) especially in regions with frequent cloud covers. In this context, combined satellite and high frequency in situ measurements represent a clear interest.

Finally, as phytoplankton species detection from pigment composition is one of the main applications of oceanic satellite-based hyperspectral measurements (Dierssen et al., 2020), the results presented here for *P. globosa* detection have broader interest. They should also benefit many other specie-specific algorithms based on second derivative of reflectance where the need for very good inter-band calibration, the recommendation to improve SNR by degrading spatial resolution (but keeping high resolution for Chl-a) and the low impact of atmospheric correction errors are all likely to be relevant. Although it is not a problem here for the spectral range 450-490 nm, imperfect correction of atmospheric absorption may be problematic in other spectral ranges.

Credit author statements

Quinten Vanhellemont processed radiometric data, applied quality controls and calculated water reflectance. Héloïse Lavigne performed *P. globosa* analysis and the impact of satellite measurement analysis. Kevin Ruddick, Quinten Vanhellemont and Héloïse Lavigne participated to the the manuscript writting.

Declaration of Competing Interest

The authors declare that they have no known competing financial interests or personal relationships that could have appeared to influence the work reported in this paper.

Data availability

Data will be made available on request.

Acknowledgements

This work has been funded by BELSPO through the Research programme for earth observation STEREO III HYPERMAQ project (contract nr SR/00/335). We thank Kevin Turpie for our exciting discussions about the main remote sensing sensor uncertainty sources. We are very grateful to the European Space Agency (ESA) for supporting the PANTHYR data processing under the HYPERNET-VN contract and for acquiring and providing CHRIS-PROBA images used for typical radiance calculations. The Flemish Marine Institute (VLIZ) and POM West-Vlaanderen are thanked for operating the PANTHYR on the RT1 Blue Innovation Platform (Ostend, Belgium) and installation support.

Appendix A. Mathematical equivalence of line height and second derivative

Algorithms for retrieving phytoplankton species or pigments from hyperspectral reflectance or absorption data include second derivative algorithms and line height algorithms, often considered as different approaches, e.g. Dierssen et al. (2021). We show here that a line height with respect to a linear baseline is mathematically equivalent to a second derivative at a single wavelength to within a multiplicative constant.

Let $y(\lambda)$ be a function of wavelength, λ, with continuous first and second derivatives. For satellite or in situ phytoplankton applications, y is typically the directional water-leaving radiance reflectance or the absorption coefficient.

The value of $y(\lambda)$ in the spectral vicinity of λ_2 can be approximated by a Taylor series (Taylor, 1715) as:

$$y(\lambda) = y(\lambda_2) + \frac{y'}{1!}(\lambda - \lambda_2)^1 + \frac{y''}{2!}(\lambda - \lambda_2)^2 + O(\lambda - \lambda_2)^3 \quad (1)$$

where y' and y'' represent the first and second derivative of y at λ_2 and O corresponds to terms of higher order (i.e. smaller terms) according to the Bachmann–Landau asymptotic notation (https://en.wikipedia.org/wiki/Big_O_notation).

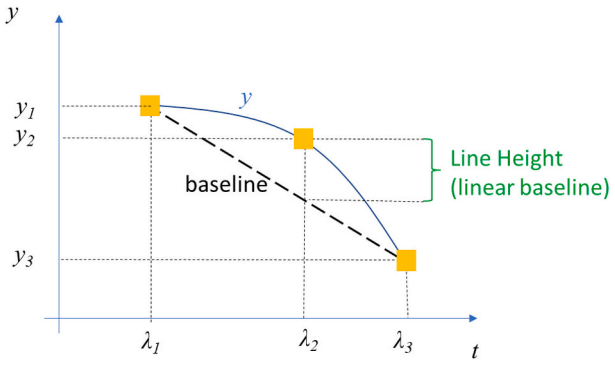

Fig. A.1. Illustration of non-centered linear baseline approach.

a) Non-centred line height

If the line height is evaluated for a wavelength, λ_2, that is not centered between the bounding wavelengths, λ_1 and λ_3, as illustrated in Fig. A.1, then the line height with respect to the linear baseline is defined as the weighted averaged:

$$yLH(\lambda_2) = y(\lambda_2) - \frac{(\lambda_3 - \lambda_2)*y(\lambda_1) + (\lambda_2 - \lambda_1)*y(\lambda_3)}{(\lambda_3 - \lambda_1)} \tag{2}$$

and Taylor approximation gives the general expression

$$yLH(\lambda_2) = y(\lambda_2) - \frac{(\lambda_3 - \lambda_2)}{(\lambda_3 - \lambda_1)}\left\{y(\lambda_2) + (\lambda_1 - \lambda_2)y' + \frac{1}{2}(\lambda_1 - \lambda_2)^2 y''\right\} - \frac{(\lambda_2 - \lambda_1)}{(\lambda_3 - \lambda_1)}\left\{y(\lambda_2) + (\lambda_3 - \lambda_2)y' + \frac{1}{2}(\lambda_3 - \lambda_2)^2 y''\right\} + O(\Delta\lambda)^3 \tag{3}$$

Which simplifies, with cancellations, to give:

$$yLH(\lambda_2) = -\frac{1}{(\lambda_3 - \lambda_1)}\frac{y''}{2}\left\{(\lambda_3 - \lambda_2)(\lambda_1 - \lambda_2)^2 + (\lambda_2 - \lambda_1)(\lambda_3 - \lambda_2)^2\right\} + O(\Delta\lambda)^3 \tag{4}$$

And with further simplification to:

$$yLH(\lambda_2) = \frac{y''}{2}(\lambda_3 - \lambda_2)(\lambda_1 - \lambda_2) + O(\Delta\lambda)^3 \tag{5}$$

Showing that the line height is proportional to the second derivative at λ_2.

b) Centred line height

In the symmetrically centered line height approach with a linear baseline, the line height is defined as:

$$yLH(\lambda_2) = y(\lambda_2) - \frac{y(\lambda_1) + y(\lambda_3)}{2} \tag{6}$$

Expressing the wavelength difference as $\Delta\lambda = \lambda_3 - \lambda_2 = \lambda_2 - \lambda_1$, substitution of the Taylor approximation (1) for $y(\lambda_1)$ and $y(\lambda_3)$ in (6) gives:

$$yLH(\lambda_2) = y(\lambda_2) - \frac{y(\lambda_2) - y'\Delta\lambda + \frac{y''}{2}\Delta\lambda^2}{2} - \frac{y(\lambda_2) + y'\Delta\lambda + \frac{y''}{2}\Delta\lambda^2}{2} + O(\Delta\lambda)^3 \tag{7}$$

Giving

$$yLH(\lambda_2) = -\frac{y''}{2}\Delta\lambda^2 + O(\Delta\lambda)^3 \tag{8}$$

Or

$$\frac{yLH(\lambda_2)}{\Delta\lambda^2} = -\frac{y''}{2} + O(\Delta\lambda)^1 \tag{9}$$

Which can be rearranged to give the well-known numerical discretization of the second derivative:

$$y'' = \frac{-2yLH(\lambda_2)}{\Delta\lambda^2} + O(\Delta\lambda) = \frac{y(\lambda_1) - 2*y(\lambda_2) + y(\lambda_3)}{\Delta\lambda^2} + O(\Delta\lambda) \tag{10}$$

A centered or non-centered line height with respect to a linear baseline is therefore mathematically equivalent to the numerical discretization of a second derivative evaluated at the line height wavelength if the same bounding wavelengths are used for the baseline algorithm and for the numerical discretization of the second derivative. The two approaches will therefore share sensitivity to noise and inter-band calibration errors and will be equivalently affected by spectral smoothing either inherent to the measurement instrument (spectral resolution FWHM) or applied explicitly in data processing. However, the baseline approach can use wavelengths with greater separation than would be normal for a simple second derivative in order to capture multiple pigments.

c) Variant approaches

Second derivative wavelength-searching algorithms which operate on a continuous range of wavelengths, e.g. searching for wavelength with maximum/minimum second derivative Lubac et al. (2008), do not have a line height equivalent.

The original Astoreca Line Height (ALH) algorithm and the Modified Astoreca Line Height (MLH) algorithms were designed with an exponentially decreasing baseline rather than a linear baseline in absorption space in order to eliminate any impact from exponentially decreasing non algal particulate and/or CDOM absorption. If the corresponding algorithms in reflectance space are expanded via Taylor approximation then these line heights are still highly sensitive to the second derivative of reflectance at the line height wavelength although the mathematical expression is more complex than a simple constant multiple of second derivative.

References

Alonso, K., Bachmann, M., Burch, K., Carmona, E., Cerra, D., De los Reyes, R., Tegler, M., 2019. Data products, quality and validation of the DLR Earth Sensing Imaging Spectrometer (DESIS). Sensors 19 (20), 4471.

Antajan, E., Chrétiennot-Dinet, M.J., Leblanc, C., Daro, M.H., Lancelot, C., 2004. 19′-hexanoyloxyfucoxanthin may not be the appropriate pigment to trace occurrence and fate of phaeocystis: the case of P. Globosa in Belgian coastal waters. J. Sea Res. 52 (3), 165–177.

Astoreca, R., Rousseau, V., Ruddick, K., Knechciak, C., Van Mol, B., Parent, J.Y., Lancelot, C., 2009. Development and application of an algorithm for detecting Phaeocystis globosa blooms in the case 2 southern North Sea waters. J. Plankton Res. 31 (3), 287–300.

Bidigare, R.R., Morrow, J.H., Kiefer, D.A., 1989. Derivative analysis of spectral absorption by photosynthetic pigments in the western Sargasso Sea. J. Mar. Res. 47 (2), 323–341.

Bidigare, R.R., Ondrusek, M.E., Morrow, J.H., Kiefer, D.A., 1990, September). In-vivo absorption properties of algal pigments. In: Ocean Optics X, Vol. 1302. International Society for Optics and Photonics, pp. 290–302.

Blauw, A.N., Los, F.J., Huisman, J., Peperzak, L., 2010. Nuisance foam events and Phaeocystis globosa blooms in dutch coastal waters analyzed with fuzzy logic. J. Mar. Syst. 83 (3–4), 115–126.

Bonato, S., Breton, E., Didry, M., Lizon, F., Cornille, V., Lécuyer, E., Christaki, U., Artigas, L.F., 2016. Spatio-temporal patterns in phytoplankton assemblages in inshore–offshore gradients using flow cytometry: a case study in the eastern English Channel. J. Mar. Syst. 156, 76–85.

Bracher, A., Bouman, H.A., Brewin, R.J., Bricaud, A., Brotas, V., Ciotti, A.M., Clementson, L., Devred, E., Di Cicco, A., Dutkiewicz, S., Wolanin, A., 2017. Obtaining phytoplankton diversity from ocean color: a scientific roadmap for future development. Front. Mar. Sci. 4, 55.

Brion, N., Jans, S., Chou, L., Rousseau, V., 2008. In: Nutrient loads to the belgian coastal zonePublished in Current status of eutrophication in the Belgian coastal zone, pp. 17–43.

Breton, E., Brunet, C., Sautour, B., Brylinski, J.M., 2000. Annual variations of phytoplankton biomass in the eastern English Channel: comparison by pigment signatures and microscopic counts. J. Plankton Res. 22 (8), 1423–1440.

Breton, E., Rousseau, V., Parent, J.Y., Ozer, J., Lancelot, C., 2006. Hydroclimatic modulation of diatom/Phaeocystis blooms in nutrient-enriched belgian coastal waters (North Sea). Limnol. Oceanogr. 51 (3), 1401–1409.

Cannizzaro, J.P., Carder, K.L., Chen, F.R., Heil, C.A., Vargo, G.A., 2008. A novel technique for detection of the toxic dinoflagellate, Karenia brevis, in the Gulf of Mexico from remotely sensed ocean color data. Cont. Shelf Res. 28 (1), 137–158.

Castagna, A., Dierssen, H., Organelli, E., Bogorad, M., Mortelmans, J., Vyverman, W., Sabbe, K., 2021. Optical detection of harmful algal blooms in the Belgian Coastal Zone: a cautionary tale of chlorophyll c3. Front. Mar. Sci. 8, 770340.

Castagna, A., Amadei Martínez, L., Bogorad, M., Daveloose, I., Dassevile, R., Dierssen, H., Beck, M., Mortelmans, J., Lavigne, H., Dogliotti, A., Doxaran, D., Rudddick, K., Vyverman, W., Sabbe, K., 2022. Dataset of optical and biogeochemical properties of diverse belgian inland and coastal waters. PANGAEA. https://doi.org/10.1594/PANGAEA.940240.

Castagna, A., Amadei Martínez, L., Bogorad, M., Daveloose, I., Dasseville, R., Dierssen, H. M., Beck, M., Mortelmans, J., Lavigne, H., Dogliotti, A., Doxaran, D., Ruddick, K., Vyverman, W., Sabbe, K., 2022. Optical and biogeochemical properties of diverse belgian inland and coastal waters. Earth Syst. Sci. Data 14, 2697–2719. https://doi.org/10.5194/essd-14-2697-2022.

Chen, Q., Mynett, A.E., 2006. Forecasting Phaeocystis globosa blooms in the dutch coast by an integrated numerical and decision tree model. Aquat. Ecosyst. Health Manag. 9 (3), 357–364.

Devred, E., Turpie, K.R., Moses, W., Klemas, V.V., Moisan, T., Babin, M., Toro-Farmer, G., Forget, M.H., Jo, Y.H., 2013. Future retrievals of water column bio-optical properties using the hyperspectral infrared imager (HyspIRI). Remote Sens. 5 (12), 6812–6837.

Dierssen, H., Bracher, A., Brando, V., Loisel, H., Ruddick, K., 2020. Data needs for hyperspectral detection of algal diversity across the globe. Oceanography 33 (1), 74–79.

Dierssen, H.M., Ackleson, S., Joyce, K., Hestir, E., Castagna, A., Lavender, S., McManus, M., 2021. Living up to the hype of hyperspectral aquatic remote sensing: science, resources and outlook. Front. Environ. Sci 9, 134.

Giardino, C., Bresciani, M., Braga, F., Fabbretto, A., Ghirardi, N., Pepe, M., Gianinetto, M., Colombo, R., Cogliati, S., Ghebrehiwot, S., Laanen, M., Peters, S., Schroeder, T., Concha, J.A., Brando, V.E., 2020. First evaluation of PRISMA level 1 data for water applications. Sensors 20 (16), 4553.

Gokul, E.A., Shanmugam, P., 2016. An optical system for detecting and describing major algal blooms in coastal and oceanic waters around India. J. Geophys. Res. Oceans 121 (6), 4097–4127.

Gons, H.J., 1999. Optical teledetection of chlorophyll a in turbid inland waters. Environ. Sci. Technol. 33 (7), 1127–1132.

Goyens, C., Ruddick, K., Kuusk, J., 2018. In: Spectral Requirements for the Development of a New Hyperspectral Radiometer Integrated in Automated Networks - the Hypernets Sensor. 9th Workshop on Hyperspectral Image and Signal Processing: Evolution in Remote Sensing (WHISPERS), pp. 1–5. https://doi.org/10.1109/WHISPERS.2018.8747259, 2018.

Gypens, N., Lacroix, G., Lancelot, C., 2007. Causes of variability in diatom and phaeocystis blooms in Belgian coastal waters between 1989 and 2003: a model study. J. Sea Res. 57 (1), 19–35.

Hoepffner, N., Sathyendranath, S., 1991. Effect of pigment composition on absorption properties of phytoplankton. Mar. Ecol. Prog. Ser. 73 (1), 11–23.

Houliez, E., Lizon, F., Thyssen, M., Artigas, L.F., Schmitt, F.G., 2012. Spectral fluorometric characterization of haptophyte dynamics using the FluoroProbe: an application in the eastern English Channel for monitoring Phaeocystis globosa. J. Plankton Res. 34 (2), 136–151.

Kou, L., Labrie, D., Chylek, P., 1993. Refractive indices of water and ice in the 0.65-to 2.5-μm spectral range. Appl. Opt. 32 (19), 3531–3540.

Kurekin, A.A., Miller, P.I., Van der Woerd, H.J., 2014. Satellite discrimination of Karenia mikimotoi and Phaeocystis harmful algal blooms in European coastal waters: merged classification of ocean colour data. Harmful Algae 31, 163–176.

Lacroix, G., Ruddick, K., Ozer, J., Lancelot, C., 2004. Modelling the impact of the Scheldt and Rhine/Meuse plumes on the salinity distribution in Belgian waters (southern North Sea). J. Sea Res. 52 (3), 149–163.

Lacroix, G., Ruddick, K., Gypens, N., Lancelot, C., 2007. Modelling the relative impact of rivers (Scheldt/Rhine/Seine) and Western Channel waters on the nutrient and diatoms/Phaeocystis distributions in Belgian waters (Southern North Sea). Cont. Shelf Res. 27 (10–11), 1422–1446.

Lancelot, C., 1995. The mucilage phenomenon in the continental coastal waters of the North Sea. Sci. Total Environ. 165 (1–3), 83–102.

Lancelot, C., Billen, G., Sournia, A., Weisse, T., Colijn, F., Veldhuis, M.J., Davies, A., Wassmann, P., 1987. Phaeocystis blooms and nutrient enrichment in the continental coastal zones of the North Sea. Ambio (1).

Lancelot, C., Keller, M., Rousseau, V., Smith Jr., W.O., Mathot Jr., S., 1998, June. Autoecology of the marine haptophyte Phaeocystis sp.. In: Physiological Ecology of Harmful Algal Blooms, 1. Springer, pp. 209–224.

Lancelot, C., Spitz, Y., Gypens, N., Ruddick, K., Becquevort, S., Rousseau, V., Lacroix, G., Billen, G., 2005. Modelling diatom and phaeocystis blooms and nutrient cycles in the southern bight of the North Sea: the MIRO model. Mar. Ecol. Prog. Ser. 289, 63–78.

Lavigne, H., Ruddick, K., 2018. The potential use of geostationary MTG/FCI to retrieve chlorophyll-a concentration at high temporal resolution for the open oceans. Int. J. Remote Sens. 39 (8), 2399–2420.

Lavigne, H., Ruddick, K., 2021. Inter-band calibration for hyperspectral water remote sensing: demonstration for CHRIS-PROBA. In: Proceedings of the IGARSS 2021 Meeting.

Lavigne, H., Vanhellemont, Q., Ruddick, K., Dogliotti, A., 2021. New processor and reference dataset for hyperspectral CHRIS-PROBA images over coastal and inland waters. In: Proceedings of the IGARSS 2021 Meeting.

Li, X., Shang, S., Lee, Z., Lin, G., Zhang, Y., Wu, J., Kang, Z., Lui, X., Yin, C., Gao, Y., 2021. Detection and biomass estimation of Phaeocystis globosa blooms off southern China from UAV-based hyperspectral measurements. IEEE Trans. Geosci. Remote Sens. 60, 1–13.

Lubac, B., Loisel, H., Guiselin, N., Astoreca, R., Felipe Artigas, L., Mériaux, X., 2008. Hyperspectral and multispectral ocean color inversions to detect Phaeocystis globosa blooms in coastal waters. J. Geophys. Res. Oceans 113 (C6).

Mannino, A., Werdell, J., Caims, B., 2017. NASA's plankton, aerosol, cloud, ocean ecosystem (PACE) mission update. https://iocs.ioccg.org/wp-content/uploads/2017/05/thu-1100-nasa-ocrt-mannino-s.pdf.

Miller, P.I., Shutler, J.D., Moore, G.F., Groom, S.B., 2006. SeaWiFS discrimination of harmful algal bloom evolution. Int. J. Remote Sens. 27 (11), 2287–2301.

Mills, D.K., Tett, P.B., Novarino, G., 1994. The spring bloom in the south western North Sea in 1989. Neth. J. Sea Res. 33 (1), 65–80.

Mizuochi, H., Tsuchida, S., Obata, K., Yamamoto, H., Yamamoto, S., 2020. Combination of cross-and inter-band radiometric calibrations for a hyperspectral sensor using model-based spectral band adjustment. Remote Sens. 12 (12), 2011.

Mobley, C.D., 1999. Estimation of the remote-sensing reflectance from above-surface measurements. Appl. Opt. 38 (36), 7442–7455.

Muylaert, K., Gonzales, R., Franck, M., Lionard, M., Van der Zee, C., Cattrijsse, A., Sabbe, K., Chou, L., Vyverman, W., 2006. Spatial variation in phytoplankton dynamics in the Belgian coastal zone of the North Sea studied by microscopy, HPLC-CHEMTAX and underway fluorescence recordings. J. Sea Res. 55 (4), 253–265.

Peperzak, L., Poelman, M., 2008. Mass mussel mortality in the Netherlands after a bloom of Phaeocystis globosa (prymnesiophyceae). J. Sea Res. 60 (3), 220–222.

Philippart, K., Blauw, A., Bolhuis, H., Brandenburg, K., Brussaard, C., Gerkema, T., Herman, P., Hommersom, A., Jacobs, P., Laanen, M., van Leeuwe, M., van den Oever, A., Peters, S., Philippart, M., Pitarch, J., Prins, T., Ruddick, K., Spaias, L., van de Waal, D., Van der Zande, D., Zuur, A., 2020. Quick Scan Zeeschuim. Rapport van het Koninklijk Nederlands Instituut voor Onderzoek der Zee (NIOZ-NWOi), Bureau Waardenburg BV, Deltares, Highland Statistics, Italian National Research Council (CNR), Koninklijk Belgisch Instituut voor Natuurwetenschappen (KBIN), Nederlands Instituut voor Ecologie (NIOO-KNAW), Rijkswaterstaat (RWS-WVL), Technische Universiteit Delft (TUD), Universiteit van Amsterdam (UvA), Universiteit Utrecht (UU), Rijksuniversiteit Groningen (RUG) & Water Insight BV. Texel, mei 2020.

Redfield, A.C., Ketchum, B.H., Richards, F.A., 1963. The influence of organisms on the composition of seawater. The sea 2, 26–77.

Rousseau, V., 2000. Dynamics of phaeocystis and diatom blooms in the eutrophicated coastal waters of the southern bight of the North Sea. Ph.D. thesis. In: Université Libre de Bruxelles, p. 205 pp;.

Rousseau, V., Becquevort, S., Parent, J.Y., Gasparini, S., Daro, M.H., Tackx, M., Lancelot, C., 2000. Trophic efficiency of the planktonic food web in a coastal ecosystem dominated by phaeocystis colonies. J. Sea Res. 43 (3–4), 357–372.

Rousseau, V., Chrétiennot-Dinet, M.J., Jacobsen, A., Verity, P., Whipple, S., 2007. The life cycle of phaeocystis: state of knowledge and presumptive role in ecology. Biogeochemistry 83 (1), 29–47.

Ruddick, K.G., Gons, H.J., Rijkeboer, M., Tilstone, G., 2001. Optical remote sensing of chlorophyll a in case 2 waters by use of an adaptive two-band algorithm with optimal error properties. Appl. Opt. 40 (21), 3575–3585.

Ruddick, K.G., De Cauwer, V., Park, Y.J., Moore, G., 2006. Seaborne measurements of near infrared water-leaving reflectance: the similarity spectrum for turbid waters. Limnol. Oceanogr. 51 (2), 1167–1179.

Schoemann, V., Becquevort, S., Stefels, J., Rousseau, V., Lancelot, C., 2005. Phaeocystis blooms in the global ocean and their controlling mechanisms: a review. J. Sea Res. 53 (1–2), 43–66.

Simis, S.G., Tijdens, M., Hoogveld, H.L., Gons, H.J., 2005. Optical changes associated with cyanobacterial bloom termination by viral lysis. J. Plankton Res. 27 (9), 937–949.

Sosik, H.M., Olson, R.J., 2007. Automated taxonomic classification of phytoplankton sampled with imaging-in-flow cytometry. Limnol. Oceanogr. Methods 5 (6), 204–216.

Stumpf, R.P., Werdell, P.J., 2010. Adjustment of ocean color sensor calibration through multi-band statistics. Opt. Express 18 (2), 401–412.

Taylor, Brook, 1715. In: Methodus Incrementorum Directa et Inversa [Direct and Reverse Methods of Incrementation] (in Latin). London, pp. 21–23 (Prop. VII, Thm. 3, Cor. 2). Translated into English in.

Van der Zande, D., Eleveld, M., Lavigne, H., Gohin, F., Pardo, S., Tilstone, G., Blauw, A., Markager, S., Enserink, L., 2019. Joint Monitoring Programme of the EUtrophication of the NOrthSea with SATellite data user case. Journal Of Operational Oceanography 12 (SI).

Van der Zande, D., Lavigne, H., Blauw, A., Prins, T.C., Desmit, X., Eleveld, M., Gohin, F., Pardo, S., Tilstone, G., Cardoso Dos Santos, J., 2019. Enhance coherence in eutrophication assessments based on chlorophyll, using satellite data as part of the EU project 'Joint monitoring programme of the eutrophication of the North Sea with satellite data'. https://www.informatiehuismarien.nl/publish/pages/162863/2_chlorophyll_satellite_data.pdf.

Vandermeulen, R.A., Mannino, A., Neeley, A., Werdell, J., Arnone, R., 2017. Determining the optimal spectral sampling frequency and uncertainty thresholds for hyperspectral remote sensing of ocean color. Opt. Express 25 (16), A785–A797.

Vanhellemont, Q., Ruddick, K., 2021. Atmospheric correction of Sentinel-3/OLCI data for mapping of suspended particulate matter and chlorophyll-a concentration in Belgian turbid coastal waters. Remote Sens. Environ. 256, 112284.

Vansteenwegen, D., Ruddick, K., Cattrijsse, A., Vanhellemont, Q., Beck, M., 2019. The pan-and-tilt hyperspectral radiometer system (PANTHYR) for autonomous satellite validation measurements—Prototype design and testing. Remote Sens. 11 (11), 1360.

Veldhuis, M.J.W., Admiraal, W., Colijn, F., 1986. Chemical and physiological changes of phytoplankton during the spring bloom, dominated by Phaeocystis pouchetii (Haptophyceae): observations in Dutch coastal waters of the North Sea. Neth. J. Sea Res. 20 (1), 49–60.

Wilson, R.T., 2013. Py6S: a python interface to the 6S radiative transfer model. Comput. Geosci. 51 (2), 166.

Zapata, M., Garrido, J.L., Jeffrey, S.W., 2006. Chlorophyll c pigments: Current status. In: Chlorophylls andBacteriochlorophylls. Springer, Dordrecht, pp. 39–53.

Zibordi, G., Mélin, F., Voss, K.J., Johnson, B.C., Franz, B.A., Kwiatkowska, E., Antoine, D., 2015. System vicarious calibration for ocean color climate change applications: requirements for in situ data. Remote Sens. Environ. 159, 361–369.